ACS APPLIED MATERIALS & INTERFACES

www.acsami.org

Research Article

# Printable and Semitransparent Nonfullerene Organic Solar Modules over 30 cm$^2$ Introducing an Energy-Level Controllable Hole Transport Layer

Yong Woon Han,[§] Hyoung Seok Lee,[§] and Doo Kyung Moon*

Cite This: https://doi.org/10.1021/acsami.1c01021

Read Online

ACCESS | Metrics & More | Article Recommendations | Supporting Information

**ABSTRACT:** For the commercialization of organic solar cells (OSCs), the fabrication of large-area modules *via* a solution process is important. The fabrication of OSCs *via* a solution process using a nonfullerene acceptor (NFA)-based photoactive layer is limited by the energetic mismatch and carrier recombination, reducing built-in potential and effective carriers. Herein, for the fabrication of high-performance NFA-based large-area OSCs and modules *via* a solution process, hybrid hole transport layers (h-HTLs) incorporating $WO_3$ and $MoO_3$ are developed. The high bond energies and electronegativities of W and Mo atoms afford changes in the electronic properties of the h-HTLs, which can allow easy control of the energy levels. The h-HTLs show matching energy levels that are suitable for both deep and low-lying highest occupied molecular orbital energy level systems with a stoichiometrically small amount of oxygen vacancies (forming $W^{6+}$ and $Mo^{6+}$ from the $W^{5+}$ and $Mo^{5+}$), affording high conductivity and good film forming properties. With the NFA-based photoactive layer, a large-area module fabricated *via* the all-printing process with an active area over 30 cm$^2$ and a high power conversion efficiency (PCE) of 8.1% is obtained. Furthermore, with the h-HTL, the fabricated semitransparent module exhibits 7.2% of PCE and 22.3% of average visible transmittance with high transparency, indicating applicable various industrial potentials.

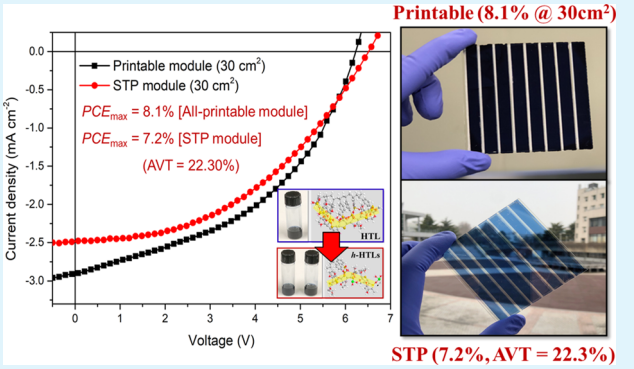


**KEYWORDS:** *nonfullerene, organic solar cell, solution process, large-area module, semitransparent module*



## 1. INTRODUCTION

Organic solar cells (OSCs) have recently attracted significant attention owing to their applications in clean energy systems and for the fabrication of large-area, flexible, and semitransparent (STP) devices *via* a simple solution process.[1−5] In particular, by employing the bulk-heterojunction structures of nonfullerene acceptor (NFA)-based photoactive materials and the development of appropriate device structures, a power conversion efficiency (PCE) of up to 18% has been achieved in recent years.[6−9] For a successful laboratory-to-fabrication (lab-to-fab) transfer, the development of photoactive materials and solution-processed devices and modules exhibiting PCEs of >20% is necessary.[10−13]

For photoactive materials, good absorption properties and moderate energy levels are important to obtain high PCEs.[14,15] In the aspect of performance factors, the short-circuit current density ($J_{SC}$), open-circuit voltage ($V_{OC}$), and fill factor (FF) contribute to the PCEs of the OSCs. The $J_{SC}$ value is related to the absorption property of the photoactive materials, and $V_{OC}$ is related to the highest occupied molecular orbital (HOMO) energy level of the photoactive donor and the lowest unoccupied molecular orbital energy level of the acceptor. High $V_{OC}$ can be achieved through the development of photoactive materials with low-lying HOMO energy levels, but this allows a narrow absorption range and good charge transport.[16−19] Therefore, an appropriate control of the combination of complementary absorption with a wide-band gap donor and low-band gap acceptor, as well as device engineering with suitable buffer layers, which can maximize the two factors in a trade-off relationship ($J_{SC}$ and $V_{OC}$), is required.[4,8,9,19−24]

In particular, a suitable coating method for the NFA-based photoactive materials and device engineering with an appropriate buffer layer allowing a solution process are necessary.[25−29] Owing to its high conductivity, transparency, and good film forming properties, poly(3,4-ethylenedioxythio-

Received: January 16, 2021
Accepted: March 19, 2021

phene) polystyrene sulfonate (PEDOT:PSS) is generally used as a hole transport layer (HTL).[30,31] In particular, in the OSCs with inverted structures for solution process applications, PEDOT:PSS (particularly, HTL Solar as a modified-PEDOT:PSS) is added to the top of the photoactive layer.[32−34] In the inverted OSCs fabricated *via* a solution process using NFA-based photoactive materials, the following critical issues may be encountered. (1) The hydrophilic PEDOT:PSS surface forms a mismatched interface with the hydrophobic surface of the photoactive layer, leading to poor film forming properties.[33,35−37] (2) Furthermore, because of the acidic and hygroscopic properties of PEDOT:PSS, the devices with PEDOT:PSS do not show long-term stability in the solution-processed devices.[32,34,35] (3) Last, the high HOMO energy level of PEDOT:PSS affords a large energy barrier with the deep and low-lying HOMO energy levels of the NFA-based photoactive donors. Therefore, in the solution-processed OSCs with PEDOT:PSS, a $V_{OC}$ drop occurs due to the energy level mismatch.[4,26] The fullerene acceptor (FA)-based photoactive donors have relatively high HOMO energy levels, leading to smaller $V_{OC}$ drop with the use of PEDOT:PSS.[38,39] However, as the typical high-performance NFA-based photoactive donors have different HOMO energy levels depending on the intended application, a large $V_{OC}$ loss may occur with the use of PEDOT:PSS. This interfacial mismatch and large $V_{OC}$ loss in the solution-processed OSCs necessitates further investigation for an efficient lab-to-fab transfer.

For a successful lab-to-fab transfer, PEDOT:PSS that can afford commercial and processing advantages is still needed. Therefore, to address the three critical limitations described previously, the development of a modified-PEDOT:PSS capable of controlling the physical and chemical properties is necessary. Metal oxides such as molybdenum oxide ($MoO_3$) and tungsten oxide ($WO_3$) have beneficial properties, such as high conductivities, easy control of physical and chemical properties, and solution processability, and have been utilized in various forms as solution-processed HTLs.[40,41] Owing to these advantages, metal oxide-doped PEDOT:PSS materials are excellent candidates for solution-processed HTL that are capable of interfacial matching and energy level control.

Luo, Ma, and co-workers reported $MoO_3$-doped PEDOT:PSS for enhancing the wettability with a photoactive film.[42] In this case, $MoO_3$ nanoparticles with good wetting properties were mixed with PEDOT:PSS to improve the wettability with the FA-based photoactive layers. In the prior studies, the development of modified-PEDOT:PSS was mainly focused on the FA system, but in real applications, additional focus should be on the NFA-based photoactive system, which requires energy level matching. Lin, Chang, and co-workers reported that the performance and stability of OSCs were enhanced through the energy level matching to that of the NFA-based photoactive donor by forming well-dispersed vanadium oxide ($VO_X$)-doped PEDOT:PSS.[34] Additionally, in our previous report, bilayer HTLs with $WO_3$ and PEDOT:PSS were introduced, which allowed energy level matching with that of the NFA-based photoactive layer, and large-area modules were developed *via* a solution process.[4] In particular, depending on the HOMO energy level of the NFA-based photoactive donor, the application of the modified-PEDOT:PSS that can minimize the $V_{OC}$ loss is required, with solution formation and development of a large-area coating technique.

Therefore, in this study, PEDOT:PSS-based universally applicable hybrid HTLs (h-HTLs) were developed using NFA-based photoactive materials with deep HOMO energy levels (SMD2 and PM6) and low-lying HOMO energy level [P(Cl−Cl)(BDD = 0.2)] *via* a solution process.[4,43] In particular, by employing $WO_3$ and $MoO_3$ precursors for the modified-PEDOT:PSS (HTL Solar), energy level control and wettability enhancement were facilitated.[44] Furthermore, formed h-HTLs exhibited energy-level variable properties by control of content concentration, indicating their applicability regardless of HOMO energy levels of the NFA-based photoactive layer. These h-HTLs showed good matching with the HOMO energy levels of the NFA-based photoactive donors. As a result, we applied h-HTLs for fabricating NFA photoactive layer-based solution processable and printable large-area modules with an active area up to 30 $cm^2$. Finally, the buffer layer-electrode structure is essential for fabricating STP-OSCs from the point of view of optical compensation. The formation of metal oxide-incorporated electrode structures which have microcavity effects is a good strategy for STP OSCs.[5] Expecting transparent properties, we also applied h-HTLs for fabricating STP large-area modules.

## 2. EXPERIMENTAL SECTION

**2.1. Materials for OSCs.** SMD2 and P(Cl−Cl)(BDD = 0.2) used as donors were synthesized by following previous literature studies.[4,41] PM6 also used as a donor was purchased from Solarmer Inc. (USA). ITIC-Th, IT-4F, and BTP-4Cl-12 used as acceptors were purchased from 1-Materials Inc. (Canada) and Solarmer Inc. (USA), respectively. Chlorobenzene (CB), 1,8-diiodooctane (DIO), and 1-chloronaphthalene (CN) used as the solvent and additives were purchased from Sigma-Aldrich (USA). Zinc acetate dehydrate, ethanolamine, and 2-methoxyethanol for precursors of sol−gel ZnO were purchased from Sigma-Aldrich (USA). Tungsten ethoxide and ammonium heptamolybdate for precursors of h-HTLs were purchased from Thermo Fisher Scientific (USA) and Sigma-Aldrich (USA), respectively. Also, isopropyl alcohol (IPA) used as the solvent of h-HTLs was purchased from Sigma-Aldrich (USA). Finally, HTL Solar for forming h-HTLs was purchased from Heraeus (Germany).

**2.2. Fabrication of (1) Solution-Processed and (2) Evaporated OSCs.** (1) The solution-processed OSCs were fabricated into an inverted structure (ITO/ZnO/photoactive layer/solution-processed HTL Solar or h-HTLs/Ag) *via* the spin-coating method. The patterned ITO glasses underwent the precleaning process in the order neutral detergent, IPA, and deionized water through the ultrasonication process. After the precleaning process, the ITO glasses were treated by ultraviolet-zone (UVO) cleaning in a UVO-cleaner (Ahtech LTS). To form ETLs, the prepared sol−gel ZnO precursor was coated onto cleaned ITO glass at 3000 rpm and then thermally annealed at 150 °C for 30 min. The photoactive layer based on SMD2/ITIT-Th (1:1.25, 20 mg $mL^{-1}$) and P(Cl−Cl)(BDD = 0.2)/IT-4F (1:1, 20 mg $mL^{-1}$) was formed with CB, and then, 0.5 vol % of DIO was added to the blend solution. Also, the photoactive layer based on PM6/BTP-4Cl-12 (1:1, 20 mg $mL^{-1}$) was formed with CB, and then, 0.5 vol % of CN was added to the blend solution. The photoactive layer of SMD2/ITIC-Th was coated onto the ZnO layer at 3000 rpm and then dried for 10 min without thermal annealing. The photoactive layer of P(Cl−Cl)(BDD = 0.2)/IT-4F was coated onto the ZnO layer at 2000 rpm and then thermally annealed at 140 °C for 10 min. Finally, the photoactive layer of PM6/BTP-4Cl-12 was coated onto the ZnO layer at 2000 rpm and then thermally annealed at 100 °C for 10 min.

The solution-processed OSCs were fabricated with h-HTLs onto the photoactive layer *via* spin coating. To form precursors of h-HTLs for a mid-HOMO energy level system, tungsten ethoxide (VI) powder was dissolved in IPA at a concentration of 1−16 mg $mL^{-1}$. To form precursors of h-HTLs for the deep HOMO energy level system,


https://doi.org/10.1021/acsami.1c01021
ACS Appl. Mater. Interfaces XXXX, XXX, XXX−XXX

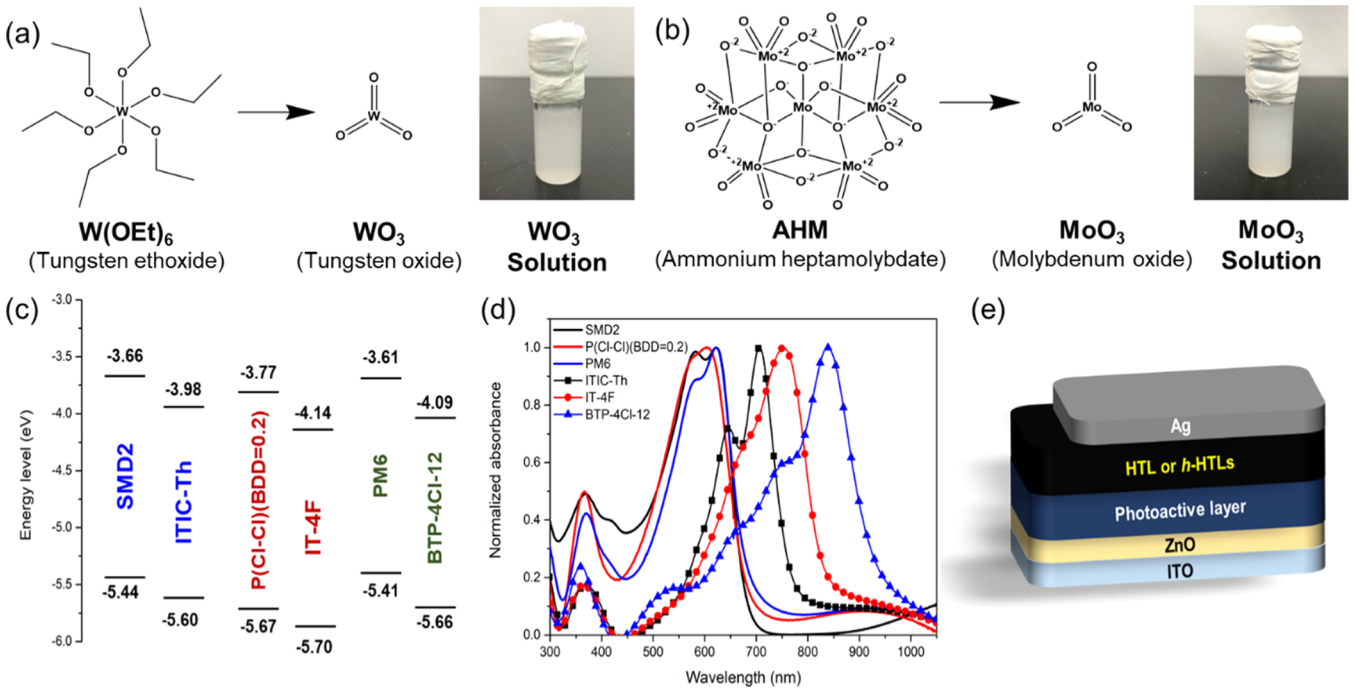


**Figure 1.** Chemical structures and formation of metal oxides, (a) $WO_3$ from tungsten ethoxide (the right image is formulated $WO_3$ solution), and (b) $MoO_3$ from ammonium heptamolybdate (the right image is formulated $MoO_3$ solution). (c) Energy-level alignments and (d) absorption properties of three pairs of donors and acceptors. (e) Structure of the fabricated device introducing pristine HTL and h-HTLs.

ammonium heptamolybdate powder was dissolved in IPA at a concentration of 0.5−2 mg $mL^{-1}$. The h-HTLs precursors were mixed with HTL Solar at various ratios for fabricating h-HTL solution. The formed h-HTL solution was coated onto the surface of the photoactive layer at 3000 rpm and then dried for 10 min without any thermal annealing. (2) The evaporated OSCs were fabricated using the same process until the photoactive layer was formed, and then, the films thermally evaporated $MoO_3$ onto the photoactive layer in a vacuum chamber (under $10^{-7}$ Torr) with a thickness of 5 nm. Finally, the top Ag electrode was formed *via* the thermal evaporation process in the vacuum chamber (under $10^{-7}$ Torr) with a thicknesses of 100 nm. The active area of the devices was 0.04 $cm^2$ with a shadow mask.

### 2.3. Fabrication of (1) Solution-Processed, (2) Printable, and (3) STP Modules.

(1) The solution-processed (spin-coating process) modules were fabricated into an inverted structure (ITO/ZnO nanoparticles/photoactive layer/solution-processed pristine HTL Solar or h-HTLs/Ag) *via* both spin coating and slot-die coating methods. The patterned ITO glasses were treated by ultrasonication and UVO cleaning. To form ETLs and photoactive layers with the spin coating method, the ZnO nanoparticles and three NFA-based photoactive solutions were coated onto ITO glass with thicknesses of 30 and 100 nm, respectively. Then, the formed h-HTL solution was coated onto the surface of photoactive layer at 3000 rpm and then dried for 10 min without any thermal annealing. To form ETLs and photoactive layers with the slot-die coating method, the ZnO nanoparticles and three NFA-based photoactive solutions were coated with a coating speed of 0.5 m $min^{-1}$ and a feed rate of 0.5 mL $min^{-1}$. Then, the formed h-HTL solution was coated onto the surface of the photoactive layer with a coating speed of 1.0 m $min^{-1}$ and a feed rate of 0.5 mL $min^{-1}$. Finally, the evaporated-Ag electrode was formed in the vacuum chamber (under $10^{-7}$ Torr) with a thickness of 100 nm.

(2) The printable modules were fabricated *via* slot-die coating with the same structure until pristine HTL or h-HTL formation of process (1) took place. To form ETLs and photoactive layers with the slot-die coating method, the ZnO nanoparticles and three NFAs-based photoactive solutions were coated with a coating speed of 0.5 m $min^{-1}$ and a feed rate of 0.5 mL $min^{-1}$. Then, the formed h-HTL solution was coated onto the surface of the photoactive layer with a coating speed of 1.0 m $min^{-1}$ and a feed rate of 0.5 mL $min^{-1}$. The printed-Ag electrode was formed using bar coating with Ag paste (opaque, TOYOTech). Consequently, the total active areas of modules were 4.7 (three cells connected) and 30.0 $cm^2$ (eight cells connected) with a shadow mask.

(3) The STP modules were fabricated *via* the spin coating process with the same structure until h-HTL formation of process (1) took place. The h-HTL solution was spin-coated onto the surface of the photoactive layer, and then, the STP electrodes were formed as follows: Au (0.03 Å $s^{-1}$, 1 nm) and Ag (1.00 Å $s^{-1}$, 15 nm).

### 2.4. Characterization of Fabricated Devices and Modules.

The absorption properties of NFA-based photoactive materials were measured using an ultraviolet−visible (UV−vis) spectrometer (Agilent 8453). The formation and chemical properties of the pristine HTL Solar and formed h-HTLs were analyzed using molecular mechanics (MM2) simulation. The energy level properties of photoactive materials were measured using ultraviolet photoelectron spectroscopy (UPS) analysis (AXIS-NOVA, Kratos). The current density−voltage ($J$−$V$) characteristics, light intensity dependences of $V_{OC}$ and $J_{SC}$, photocurrent density characteristics, and dark $J$−$V$ characteristics of fabricated devices were measured using a power source meter (Keithley 2400) and a solar simulator (Oriel, AM1.5G calibrated Xe and LED lamps). For improved reliability of devices and modules, the $J$−$V$ characteristics were measured with a source measurement unit in a four-wire configuration. The external quantum efficiency (EQE) characteristics of fabricated devices were measured with an incident PCE (Polaronix K3100, Mc Science). The X-ray photoelectron spectroscopy (XPS) characteristics of the pristine HTL Solar and h-HTLs were studied using ULVAC-PHI 5000 VersaProbe (ULVAC). The current−voltage ($I$−$V$) characteristics and conductivity characteristics were measured using a four-point probe station (Mc Science). The surface contact angle and surface energy characteristics were analyzed using a contact-angle analyzer (DSA100, KRUSS). The surface morphology characteristics were analyzed using


https://doi.org/10.1021/acsami.1c01021
ACS Appl. Mater. Interfaces XXXX, XXX, XXX−XXX

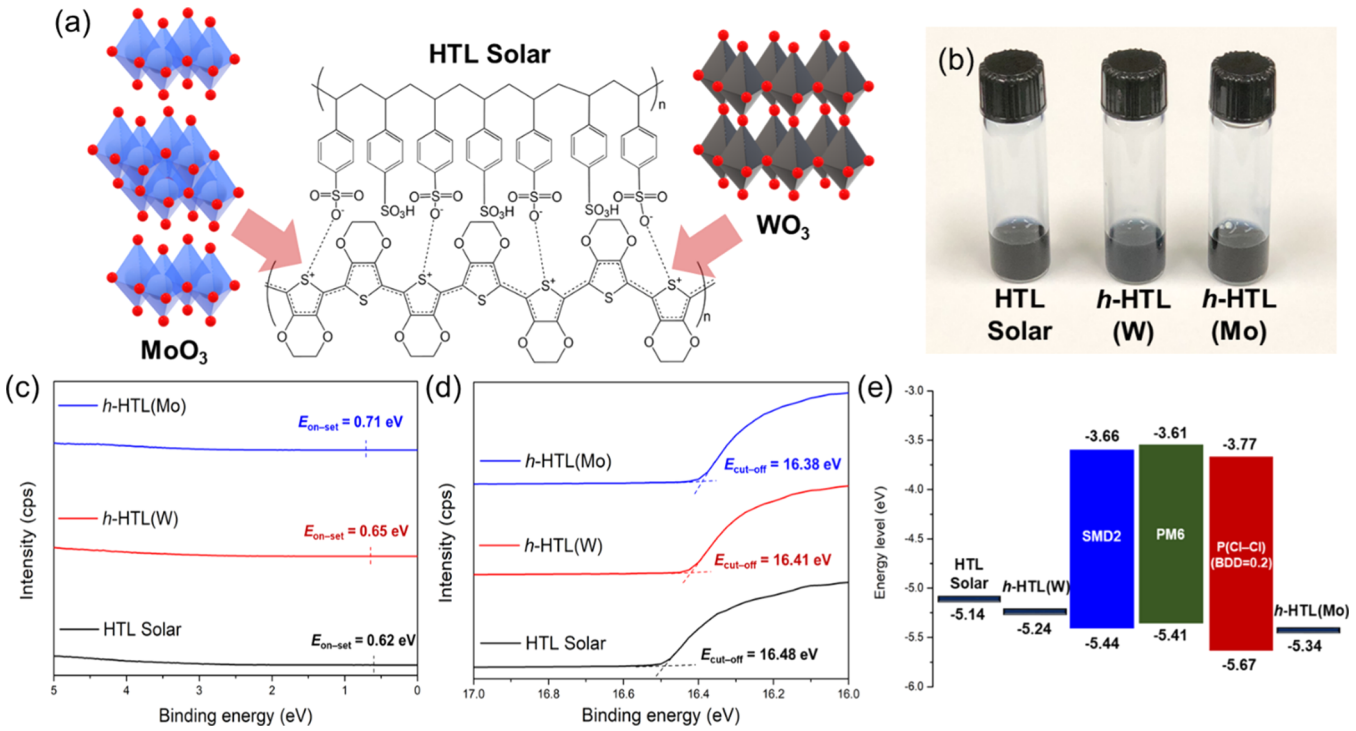


**Figure 2.** (a) Molecular structure of HTL Solar and formation of h-HTLs incorporating $WO_3$ and $MoO_3$ materials, (b) images of formed HTL solutions in the order HTL Solar, h-HTL(W), and h-HTL(Mo). UPS characteristics of HTLs (c) cut-off energy and (d) on-set energy and (e) calculated energy level alignments of HTLs and three donors.

an atomic force microscope (PSIA XE-100, Park Systems). The crystalline structures were characterized using grazing-incidence wide-angle X-ray scattering analysis (GIWAXS) measurement on the 3C beamline at the Pohang Accelerator Laboratory (PAL).

## 3. RESULTS AND DISCUSSION

**3.1. Properties of the Photoactive Layer and Formation of h-HTLs.** For the fabrication of high-performance OSCs *via* a solution process, SMD2, P(Cl−Cl)(BDD = 0.2), and PM6, which are the donor polymers that are well matched with the NFAs, were used (Figure S1a−c). The chemical structures and images of the solutions of the precursors and formulated metal oxides used to form the h-HTLs are shown in Figure 1a,b. SMD2, P(Cl−Cl)(BDD = 0.2), and PM6 showed the HOMO energy levels at −5.44, −5.67, and −5.41 eV and band gap energy levels of 1.78, 1.80, and 1.94 eV (Figure 1c). These values were consistent with the optical band gap energies calculated from the Tauc plot (Figure S2). Both SMD2 and PM6 showed deep HOMO levels and low band gap energies (1.78 and 1.80 eV, respectively) and exhibited absorption in the 500−700 nm region (Figure 1g). In addition, P(Cl−Cl)(BDD = 0.2) showed low-lying HOMO energy levels and a medium band gap (1.90 eV) with slightly blue-shifted absorption ($\lambda$ = 500−680 nm) (Figure 1d). The photoactive layers were formed by utilizing optimal NFAs, considering the optoelectronic properties and energy levels of each donor polymer. As shown in Figure 1e, the devices with an inverted structure (ITO/ZnO/photoactive layer/HTL solar or h-HTLs/Ag) were fabricated *via* the solution process.

**3.2. Energy-Level Alignments of the Photoactive Layer and h-HTLs.** Generally in PEDOT:PSS, the PEDOT and PSS chains show Coulombic interactions. In particular, the interaction occurs between the highly positively charged sulfur ion of PEDOT, which has a conjugated thiophene-based structure and the negatively charged oxygen ion of PSS (Figure 2a).[45,46] By introducing the screening effect through PSS removal and enhancing the crystalline structures of PEDOT molecules, the conductivity of PEDOT:PSS can be increased.[47−49] For the energy-level modification of HTL Solar, we applied tungsten ethoxide and ammonium heptamolybdate as precursors of $WO_3$ and $MoO_3$ to HTL Solar, and h-HTL solutions [referred as h-HTL(W) and h-HTL(Mo)] were prepared. These formed octahedral cubic structures with the oxygen array around the core metal atom and stable $WO_3$ sharing the edges and forming a pseudocubic structure, while $MoO_3$ shared the corners and edges, forming an orthorhombic polymorph structure (Figure 2a).[50−52] These metal oxide precursors can be chemically converted into metal oxides ($WO_3$ in a stable $\gamma$-$WO_3$ phase and $MoO_3$ in a stable $\alpha$-$MoO_3$ phase) *via* a sol−gel process in an alcoholic solvent.[50,52,53] The metal oxide precursors were mixed with HTL Solar to form the h-HTL solution, which showed similar dark-blue color and viscosity as those of HTL Solar (Figure 2b).

The formation tendencies and chemical properties of the pristine HTL Solar and h-HTLs were analyzed using molecular mechanics (MM2) simulation (Figure S3). The PSS chain, $WO_3$, and $MoO_3$ were randomly arranged along with the PEDOT chain, and the molecular behaviors were calculated in terms of the steric hindrance and torsion angle. As a result of simulation, pristine HTL Solar was predicted to form a relatively bent structure with a total energy of approximately 2909.06 kcal $mol^{-1}$ and a torsion angle of 448.98° (Figure S3a). In contrast, h-HTL(W) exhibited a low total energy of 1631.94 kcal $mol^{-1}$ and a torsion angle of 393.23°, showing a relatively planar and stable molecular structure incorporating $WO_3$ (Figure S3b). Furthermore, h-HTL(Mo) showed the


https://doi.org/10.1021/acsami.1c01021
ACS Appl. Mater. Interfaces XXXX, XXX, XXX−XXX

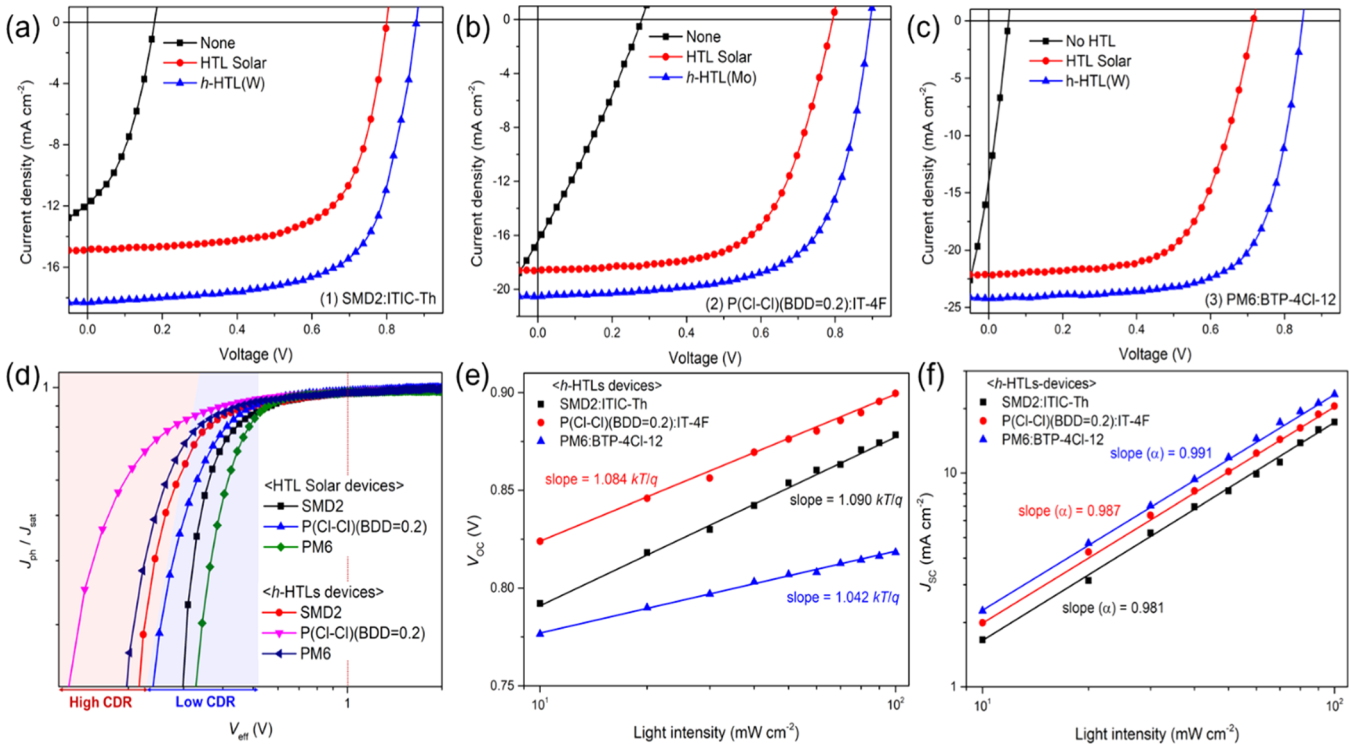


**Figure 3.** $J-V$ characteristics of fabricated devices introducing various HTLs based on the photoactive layer of (a) SMD2/ITIC-Th, (b) P(Cl−Cl)(BDD = 0.2)/IT-4F, and (c) PM6/BTP-4Cl-12. (d) Carrier dissociation probability (CDP) characteristics calculated from photocurrent density−effective voltage ($J_{ph}-V_{eff}$) characteristics (marked CDR means carrier dissociation region). (e) $V_{OC}$−light intensity, and (f) $J_{SC}$−light intensity dependence characteristics of fabricated devices introducing h-HTLs (SMD2 and PM6) with h-HTL(W), and P(Cl−Cl)(BDD = 0.2) with h-HTL(Mo).

**Table 1. Photovoltaic Performances of Solution-Processed Devices Introduced Based on SMD2 and P(Cl−Cl)(BDD = 0.2) and PM6 Introducing h-HTLs under Optimal Process Conditions**[a]

| BHJ layer | HTLs | $J_{SC}$ [mA cm$^{-2}$] | $V_{OC}$ [V] | FF [ %] | $PCE_{max}$[b] [%] | calc. $J_{SC}$ [mA cm$^{-2}$] | $R_{Sh}$[c] [Ω cm$^2$] | $R_S$[c] [Ω cm$^2$] |
|---|---|---|---|---|---|---|---|---|
| SMD2[d]/ITIC-Th | none | 12.1 (11.6 ± 0.52) | 0.171 (0.160 ± 0.01) | 40.1 (39.7 ± 0.37) | 0.831 | 10.00 | 17.3 | 7.5 |
| | HTL Solar | 14.9 (14.6 ± 0.31) | 0.798 (0.780 ± 0.02) | 66.4 (66.1 ± 0.29) | 8.1 | 12.96 | 945.6 | 5.8 |
| | h-HTL(W) | 18.3 (18.1 ± 0.19) | 0.878 (0.868 ± 0.01) | 67.0 (66.9 ± 0.14) | 10.8 | 16.02 | 993.1 | 5.4 |
| P(Cl−Cl)(BDD = 0.2)[e] /IT-4F | none | 16.9 (16.3 ± 0.63) | 0.272 (0.261 ± 0.01) | 27.9 (27.5 ± 0.42) | 1.3 | 11.92 | 19.0 | 7.3 |
| | HTL Solar | 18.6 (18.0 ± 0.33) | 0.798 (0.780 ± 0.01) | 61.7 (61.5 ± 0.24) | 9.2 | 16.12 | 1095.2 | 6.7 |
| | h-HTL(Mo) | 20.5 (20.3 ± 0.20) | 0.899 (0.889 ± 0.01) | 65.9 (65.8 ± 0.12) | 12.2 | 18.53 | 1212.8 | 4.9 |
| PM6[f]/BTP-4Cl-12 | none | 16.1 (15.7 ± 0.49) | 0.050 (0.030 ± 0.02) | 25.1 (24.8 ± 0.34) | 0.2 | 13.32 | 2.8 | 4.5 |
| | HTL Solar | 22.0 (21.6 ± 0.37) | 0.717 (0.707 ± 0.01) | 64.6 (64.3 ± 0.30) | 10.2 | 20.21 | 1030.1 | 3.9 |
| | h-HTL(W) | 24.2 (24.0 ± 0.19) | 0.858 (0.838 ± 0.02) | 68.4 (68.3 ± 0.10) | 14.2 | 22.23 | 1430.4 | 3.5 |

[a]Devices were fabricated with an inverted structure (ITO/ZnO/photoactive layer/solution-processed HTLs/Ag, active area of 0.04 cm$^2$). [b]Maximum value was obtained from the best performance among 10 fabricated devices. [c]$R_{Sh}$ and $R_S$ were calculated in the equivalent circuit. [d]SMD2-based devices exhibited the best performance when composed of ITIC-Th (dried for 10 min without additional thermal treatment). [e]P(Cl−Cl)(BDD = 0.2)-based devices exhibited the best performance when composed of IT-4F (thermal treatment at 140 °C for 10 min). [f]PM6-based devices exhibited the best performance when composed of BTP-4Cl-12 (thermal treatment at 100 °C for 10 min).

lowest total energy of 1467.32 kcal mol$^{-1}$ and a torsion angle of 249.88°, affording a more planar and stable molecular structure incorporating $MoO_3$ (Figure S3c). The MM2 simulation results showed low values of the torsion angle and total energy in the order HTL Solar > h-HTL(W) > HTL(Mo), affording a more stable molecular structure.

Metal oxides incorporated in HTL Solar resulted in an energy level shift and increase in conductivity through the partial redox reaction with the PEDOT chain.[54] In particular,


https://doi.org/10.1021/acsami.1c01021
ACS Appl. Mater. Interfaces XXXX, XXX, XXX−XXX

owing to the strong bonding of tungsten and molybdenum with the oxygen atoms, negatively charged oxygen atoms interacted with the sulfur ions of the PEDOT chain. In terms of $MoO_3$ and $WO_3$, $WO_3$ shows a higher bond dissociation energy than $MoO_3$ (W−O: 720 ± 71 kJ $mol^{-1}$ vs Mo−O: 502 kJ $mol^{-1}$).[55] Because of the binding between metal−oxygen atoms, partial electronegativities were induced in the oxygen atoms of metal oxides, and the interactions occurred with the positively charged sulfur atoms in the PEDOT chain. Furthermore, owing to the relatively low binding energy of $MoO_3$, stronger interactions occurred among the sulfur atoms of PEDOT and oxygen atoms of the metal oxide, and lower torsion angle and stable molecular structures were observed with h-HTL(Mo) than with h-HTL(W).

The energy levels and images of the alignments of HTLs determined by UPS are shown in Figure 2c−e. The calculated HOMO energy levels were −5.14 eV ($E_{cut\text{-}off}$ = 16.48 eV and $E_{on\text{-}set}$ = 0.62 eV) of the pristine HTL Solar, −5.24 eV ($E_{cut\text{-}off}$ = 16.41 eV and $E_{on\text{-}set}$ = 0.65 eV) for h-HTL(W), and −5.34 eV ($E_{cut\text{-}off}$ = 16.38 eV and $E_{on\text{-}set}$ = 0.71 eV) for h-HTL(Mo). These results were consistent with the MM2 calculation results, indicating that stable molecular structures were formed with h-HTL(W) and h-HTL(Mo). As a result, the formation of h-HTLs resulted in the energy level modification of pristine HTL Solar. These results provide an effective strategy to address the energy level mismatch encountered with the NFA-based photoactive donors used in this study *via* the solution process (Figure 2e).

**3.3. Photovoltaic Properties.** The current density−voltage ($J$−$V$) curves and photovoltaic properties of the devices fabricated using HTLs with various photoactive layers are shown in Figure 3a−c and Table 1. Additionally, the photovoltaic properties of devices incorporating e-$MoO_3$ are shown in Table S1. In the case of the SMD2/ITIC-Th-based photoactive layer (deep HOMO energy level of the donor), a maximum PCE of 10.8% ($J_{SC}$ = 18.3 mA $cm^{-2}$, $V_{OC}$ = 0.878 V, and FF = 67.0%) was obtained using h-HTL(W). This value was higher than that of the pristine HTL Solar incorporating device (8.1%). In the case of P(Cl−Cl)(BDD = 0.2)/IT-4F-based photoactive layer (low-lying HOMO energy level of the donor), a maximum PCE of 12.2% ($J_{SC}$ = 20.5 mA $cm^{-2}$, $V_{OC}$ = 0.899 V, and FF = 65.9%) was obtained for the h-HTL(Mo)-based device, affording a higher value than that of the pristine HTL Solar-based device (9.2%). Furthermore, for the PM6/BTP-4Cl-12-based photoactive layer (deep HOMO energy level of the donor), similar to the case of SMD2, a maximum PCE of 14.2% ($J_{SC}$ = 24.2 mA $cm^{-2}$, $V_{OC}$ = 0.858 V, and FF = 68.4%) was obtained for the h-HTL(W)-containing devices, thereby affording the best performance. These results showed similar values of $J_{SC}$ and $V_{OC}$ and a slightly lower FF value compared to those for the devices with e-$MoO_3$, the commercial HTL (Figure S4 and Table S1). In other words, the issue of $V_{OC}$ drop was resolved in the solution-processed devices, and a high current density values were achieved.

Therefore, the $J_{SC}$, $V_{OC}$, and FF values were improved in the h-HTL(W)-containing devices with the SMD2 and PM6 systems with deep HOMO energy levels as well as in the h-HTL(Mo)-containing devices with the P(Cl−Cl)(BDD = 0.2) system with a low-lying HOMO energy level. This was because the use of h-HTLs allowed a well-matched energy level alignment between the NFA-based photoactive donors and paired h-HTLs, leading to enhanced internal built-in potential.[56,57] The apparent energy level alignments were analyzed through UPS measurements by applying HTLs to the photoactive layers (Figures S5−S7). As pristine HTL Solar was used, the SMD2/ITIC-Th- and PM6/BTP-4Cl-12-based photoactive layers with the deep HOMO energy levels showed larger energy barriers compared to those of the pristine photoactive layers. The introduction of pristine HTL Solar onto SMD2 and PM6-based photoactive layer showed higher hole injection barriers due to energy level mismatch between donor and HTL Solar (Figure 2e). However, with the incorporation of h-HTL(W), the lowest energetic barriers were observed with the photoactive layer, leading to well-matched energy levels and improved $J_{SC}$ and $V_{OC}$ (Figures S5 and S6). Similarly, for the P(Cl−Cl)(BDD = 0.2)/IT-4F-based photoactive layer with low-lying HOMO energy levels, the application of the h-HTL(Mo) led to the formation of optimized energetic barriers, affording well-matched energy levels (Figure S7).

In contrast, the introduction of other h-HTLs (not matched) resulted in slightly inferior performances than those of the donor and h-HTL-matched combinations [SMD2 and PM6 with h-HTL(W) and P(Cl−Cl)(BDD = 0.2) with h-HTL(Mo)], as shown in Table S2. However, the favorable energy-level matching was achieved through the concentration control of the h-HTLs. The $J$−$V$ curves and photovoltaic properties with the variation in the concentration of the h-HTL contents are shown in Figures S8−S10 and Tables S3−S8. In the SMD2 and PM6 systems, the h-HTL(W) showed the best matching, but when h-HTLs(Mo) were introduced, some well-matched alignments with maximum $V_{OC}$ were also observed (Figures S8 and S9 and Tables S3−S6). The optimal concentrations of the h-HTL(W) were different for the SMD2 and PM6 systems with values of 4 and 2 w/w %, respectively, and those of the h-HTL(Mo) were 0.5 and 1 w/w %, respectively. These were because PM6 showed slightly higher HOMO energy levels than those of SMD2. Additionally, in the P(Cl−Cl)(BDD = 0.2) system, comparable $V_{OC}$ and PCE values were obtained not only with the h-HTLs(Mo) but also with a high concentration (16 w/w %) of h-HTLs(W) (Figure S10 and Tables S7−S8). These results indicate that by varying the contents, h-HTLs afford universal characteristics of well-matched alignment with the NFA-based photoactive layers, regardless of HOMO energy levels.

The EQEs and calculated $J_{SC}$ (cal. $J_{SC}$) values of the fabricated devices are shown in Figure S11a−c and Table 1. With the application of pristine HTL Solar and h-HTLs, improved EQE values were achieved in a wide range of wavelengths (at $\lambda$ = 350−900 nm) compared to those for the devices without the HTLs. In the devices with h-HTLs, the values of calculated $J_{SC}$ were 16.02, 18.53, and 22.23 mA $cm^{-2}$ for SMD2, P(Cl−Cl)(BDD = 0.2), and PM6, respectively, exhibiting a similar trend with the increase of $J_{SC}$ values from Table 1. This result was attributed to the effective carrier dissociation induced by the well-matched energy level alignment of the NFA-based photoactive layer and h-HTL.[58] Furthermore, at 450−800 nm, the devices with h-HTLs showed slightly lower EQE values compared to those with e-$MoO_3$. These results exhibited that despite the presence of surface vacancies and occurrence of carrier recombination in the devices fabricated *via* the solution process, the h-HTLs were comparable to those of the devices fabricated by evaporation (Figure S12).[59]

**3.4. Carrier Dissociation Properties and FF.** After introducing pristine HTL Solar and h-HTLs, CDP was


https://doi.org/10.1021/acsami.1c01021
ACS Appl. Mater. Interfaces XXXX, XXX, XXX−XXX

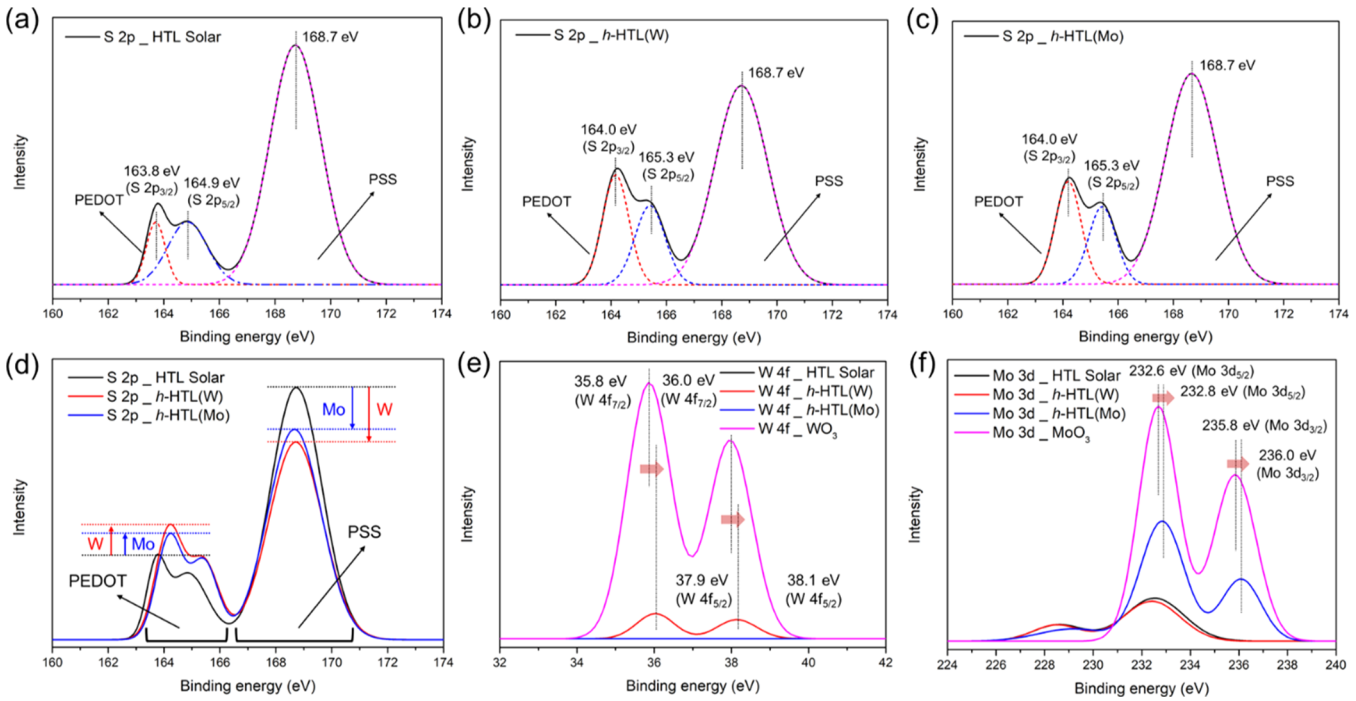


**Figure 4.** Surface XPS characteristics of HTL films. S 2p atomic signals of (a) pristine HTL Solar, (b) h-HTL(W), (c) h-HTL(Mo), and (d) three HTLs. (e) W 4f atomic signals and (f) Mo 3d atomic signals of HTLs against pristine metal oxides.

analyzed through photocurrent density−effective voltage ($J_{ph}$−$V_{eff}$) measurements (Figure 3d). The saturated photocurrent and normal photocurrent density were calculated through measurements under illumination and dark conditions. The h-HTL-containing devices showed higher $J_{ph}$ values than the pristine HTL Solar-containing devices, and fast saturation was observed at a $V_{eff}$ of approximately 0.7 V (Figures 3d and S13). With the use of pristine HTL Solar and optimized h-HTLs, carrier dissociation probabilities of 96.28 and 96.54%, respectively, in the SMD2-based devices, 97.74 and 97.87%, respectively, in the P(Cl−Cl)(BDD = 0.2)-based devices, and 95.91 and 97.02%, respectively, were observed in the PM6-based devices (at a $V_{eff}$ of approximately 1 V). As a result, the h-HTL-containing devices showed a tendency toward fast saturation, exhibiting high carrier dissociation tendency [in high carrier dissociation region (CDR)]. In contrast, pristine HTL Solar-containing devices exhibited low carrier dissociation tendency (in low CDR) with slow saturation at high $V_{eff}$. As a result, the h-HTLs induced efficient carrier dissociation, which consequently contributed toward increases in the $J_{SC}$ and FF values.[60,61]

With the measurement of the dependence of $V_{OC}$ and $J_{SC}$ under various illumination conditions, the carrier recombination properties of the pristine HTL Solar and h-HTL-incorporating devices were analyzed (Figures 3e,f and S14). For light intensity ($I$), the relationship of $V_{OC} \propto kT/q \ln(I)$ is satisfied.[62,63] As optimum h-HTLs were introduced in the SMD2, P(Cl−Cl)(BDD = 0.2), and PM6-based photoactive layers, the slope values were $1.090kT/q$, $1.084kT/q$, and $1.042kT/q$, respectively. Also, pristine HTL Solar was introduced as above, the slope values were $1.154kT/q$, $1.134kT/q$, and $1.107kT/q$, respectively. Additionally, the power-law relationship of $J_{SC} \propto I^{\alpha}$ is fulfilled.[64] As optimum h-HTLs were introduced in the SMD2, P(Cl−Cl)(BDD = 0.2), and PM6-based photoactive layers, the slope ($\alpha$) values were 0.981, 0.987, and 0.991, respectively. Also, pristine HTL Solar was introduced as above, and the slope ($\alpha$) values were 0.968, 0.795, and 0.983, respectively. In general, when the slope values of $kT/q$ are closer to 1.0, suppressed trap-assisted recombination is observed, and when the slope value of $\alpha$ is closer to 1.0, suppressed bimolecular recombination is exhibited.[62−64] The h-HTL-incorporating devices showed excellent dependent property with suppressed carrier recombination properties. Furthermore, the measurement of dark $J$−$V$ curves of the fabricated devices showed a low leakage current under reverse bias and high current density under forward bias for the h-HTL-incorporating devices (Figure S15). Consequently, with the introduction of h-HTLs, well-matched energy level alignments were formed, affording efficient carrier dissociation and suppressed carrier recombination. Therefore, $J_{SC}$ and FF were significantly improved with lowest variation values as shown in Table 1, indicating higher reliabilility.[65]

### 3.5. Atomic Signals and Conductivity Measurement.

The surface XPS properties of the pristine HTL Solar and h-HTLs are shown in Figures 4 and S16. With the formation of h-HTLs, the carbon (C 1s) atomic signals decreased due to an increase of the metal oxide content (Figure S16a). The oxygen (O 1s) atomic signals of h-HTLs showed a peak shift of approximately 0.2 eV compared to the peak of the pristine HTL Solar (532.1 eV: C−O peak; Figures S16b and S17). Due to the formation of the h-HTLs, the O 1s atomic signal peaks of the PEDOT molecules became more enhanced compared to those of the PSS molecules (Figure S17b,c).[66] In contrast, as shown in Figure 4a−c, the sulfur (S 2p) atomic signals of the pristine HTL Solar and h-HTLs showed the typical peaks of PEDOT (approximately 163.9 and 165.1 eV for S $2p_{3/2}$ and S $2p_{1/2}$ peaks, respectively) and PSS (168.7 eV for sulfur of thiophene) molecules.[67,68] With the use of $WO_3$ and $MoO_3$, PSS peaks decreased significantly [h-HTL(W): 21.66% decrease; h-HTL(Mo): 16.57% decrease], and PEDOT peaks increased considerably [h-HTL(W): 26.03% increase; h-HTL(Mo): 33.26% increase] (Figure 4a−d). With the


https://doi.org/10.1021/acsami.1c01021
ACS Appl. Mater. Interfaces XXXX, XXX, XXX−XXX

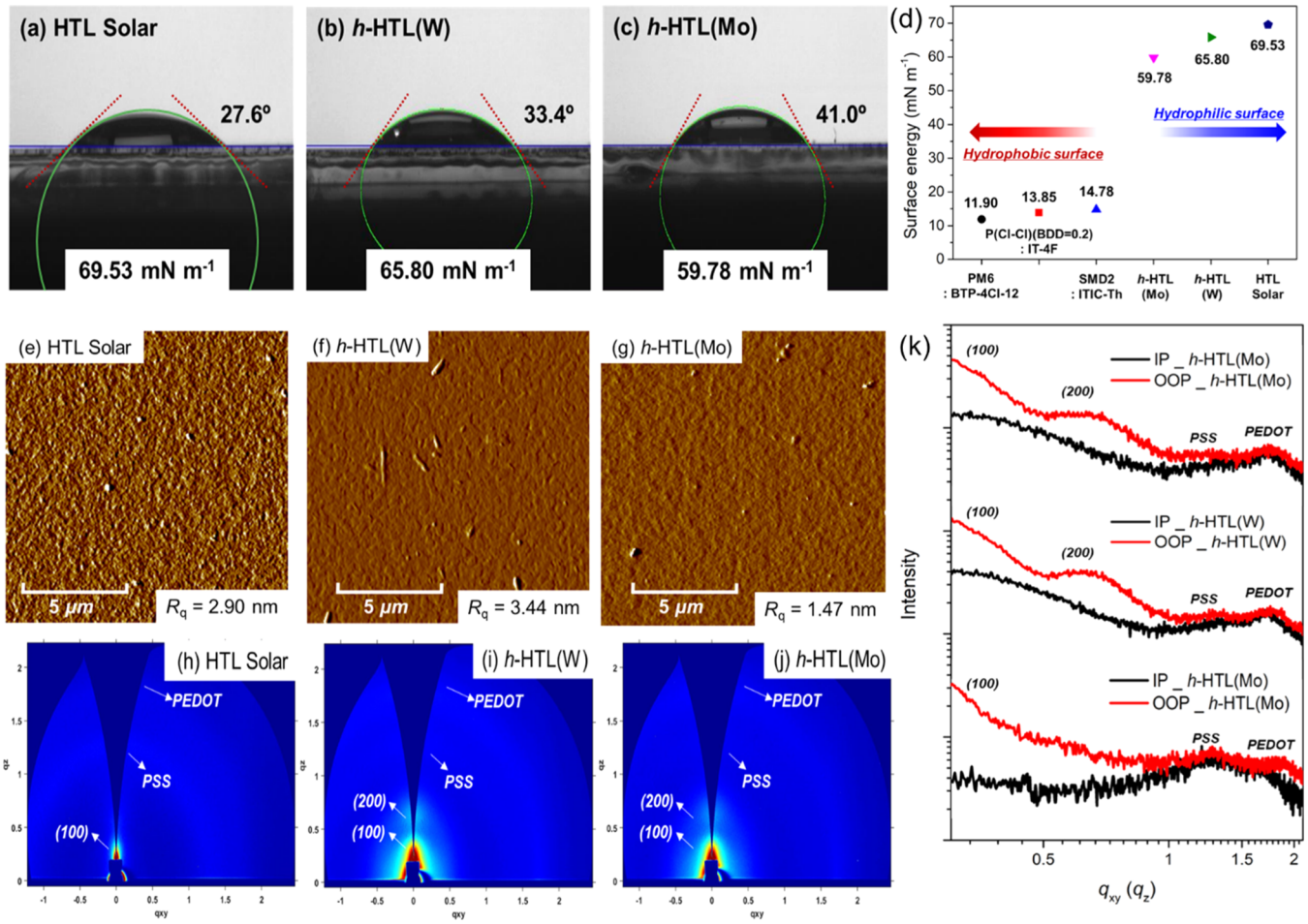


**Figure 5.** Contact angle and surface energy characteristics of (a) HTL Solar, (b) h-HTL(W), and (c) h-HTL(Mo) films, and (d) surface energy graph of photoactive layers and HTLs. The surface morphology characteristics of (e) HTL Solar, (f) h-HTL(W), and (g) h-HTL(Mo) films. The GIWAXS characteristics of (h) HTL Solar, (i) h-HTL(W), and (j) h-HTL(Mo) films, and (k) line-cut profile characteristics of HTL films along the in-plane (IP) and out-of-plane (OOP) directions.

formation of h-HTLs, the stacking of the PEDOT molecules was enhanced, inducing the screen effect of the PSS molecules and a consequent increase in conductivity. Furthermore, the electrical resistivity and conductivity properties obtained through the four-probe measurements were 5.657 Ωm and 0.176 S $m^{-1}$, 4.718 Ωm and 0.212 S $m^{-1}$, and 3.424 Ωm and 0.292 S $m^{-1}$ for pristine HTL Solar, h-HTL(W), and h-HTL(Mo), respectively. As a result, conductivity properties were significantly enhanced with the formation of h-HTLs, resulting to be favorable for enhanced carrier transport (Figure S18).

The formation of h-HTL(W) afforded a shift in the peaks (36.0 and 38.1 eV for W $4f_{7/2}$ and W $4f_{5/2}$ peaks, respectively) compared to the typical peaks of pristine $WO_3$ (35.8 and 37.9 eV for W $4f_{7/2}$ and W $4f_{5/2}$ peaks, respectively) (Figure 4e). Similarly, the formation of h-HTL(Mo) also showed peak shifts (232.8 and 236.0 eV for Mo $3d_{5/2}$ and Mo $3d_{3/2}$, respectively) compared to the typical peaks of pristine $MoO_3$ (232.6 and 235.8 eV for Mo $3d_{5/2}$ and Mo $3d_{3/2}$, respectively) (Figure 4f). These results were because effective conversion occurred from $W^{5+}$ and $Mo^{5+}$ structures formed by solution-processed HTLs to $W^{6+}$ and $Mo^{6+}$ structures containing stoichiometrically small amounts of oxygen vacancies. The appropriate oxygen vacancies with n-doping are important for the conductivities of $WO_3$ and $MoO_3$.[69−71] Consequently, the changes in the energy levels and enhancement in conductivity of the h-HTLs were results of the modification of electronic structures by hybridization.

**3.6. Surface Morphology and Crystalline Characteristics.** The surface and crystalline properties of the h-HTLs are also directly related to the electronic structures. The surface contact angles and surface energies of various HTLs are shown in Figures 5a−d and S19. For the pristine HTL Solar, a contact angle of 27.6° and a surface energy of 69.53 mN $m^{-1}$ were obtained, while for h-HTL(W) and h-HTL(Mo), the contact angles and surface energies were 33.4° and 65.80 mN $m^{-1}$ and 41.0° and 59.78 mN $m^{-1}$, respectively. In general, superior interfacial contact is observed at the junctions with similar surface energies.[72,73] As shown in Figure S19, even after the HTLs were introduced on the photoactive layer, the h-HTL films showed higher contact angles and lower surface energies than the pristine HTL Solar film. In other words, the introduction of h-HTLs showed more hydrophobic surfaces than pristine HTL Solar film. As a result, good interfacial contact with the photoactive layers was formed with the introduction of h-HTLs.

The surface morphologies of different HTLs are shown in Figure 5e−g. The pristine HTL Solar film showed a root-mean-square (RMS) roughness ($R_q$) of approximately 2.90 nm, indicating a relatively rough surface (Figure 5e). In


https://doi.org/10.1021/acsami.1c01021
ACS Appl. Mater. Interfaces XXXX, XXX, XXX−XXX

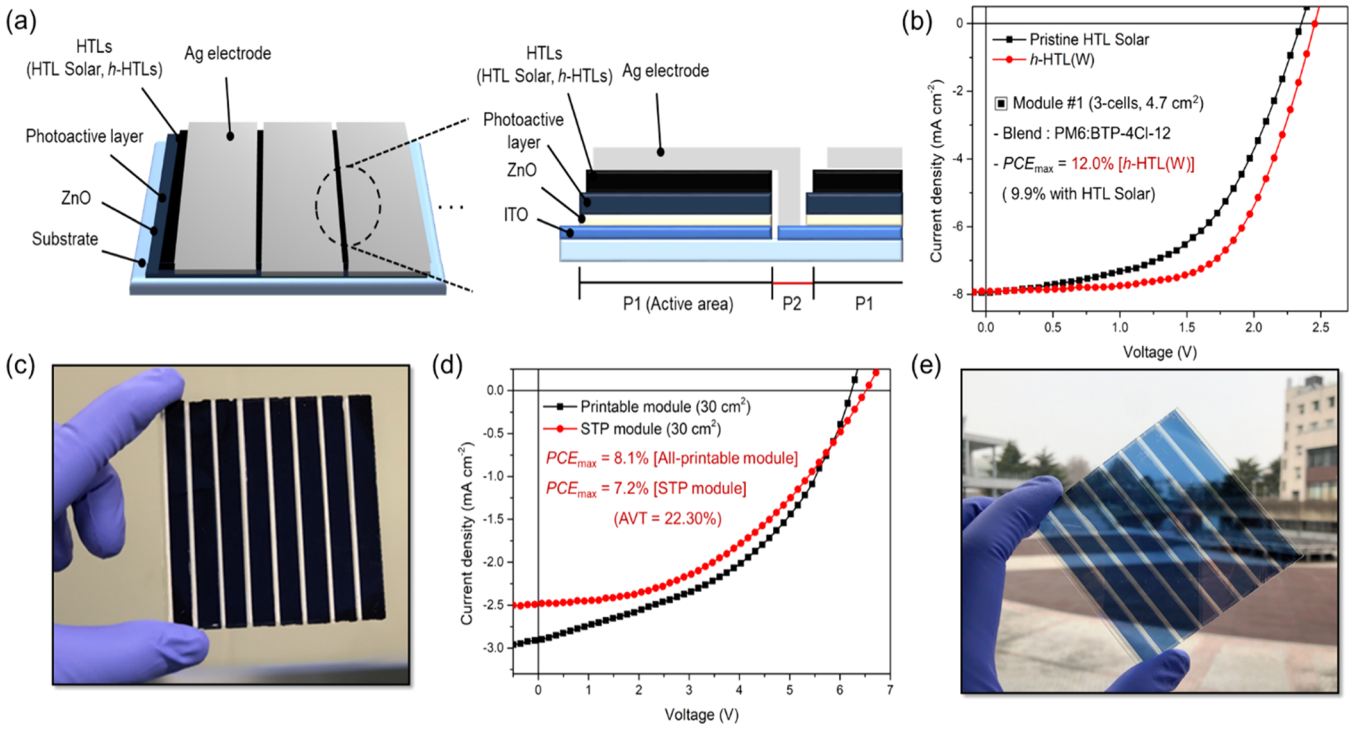


**Figure 6.** Universal application of h-HTLs for solution-processed large-area modules. (a) Schematic images of fabricated large-area modules (active area of 4.7−30.0 $cm^2$ with 3∼8-cell connected modules, P1 is the active area and P2 is the dead area of modules). (b) PM6/BTP-4Cl-12 (module #1, active area of 4.7 $cm^2$) introducing pristine HTL Solar and h-HTL(W). (c) Picture of fabricated printable modules with a printed-Ag electrode (active area of 30 $cm^2$). (d) Photovoltaic characteristics of fabricated modules with h-HTL(W) and printed-Ag (printable modules) and STP modules based on the photoactive layer of PM6/BTP-4Cl-12 (active area of 30 $cm^2$). (e) Picture of fabricated STP modules *via* the solution process (active area of 30 $cm^2$).

**Table 2. Photovoltaic Performances of Solution-Processed Modules Introduced Based on PM6 and P(Cl−Cl)(BDD = 0.2) Introducing h-HTLs under Optimal Process Conditions[a]**

| BHJ layer | area [$cm^2$] | HTLs | $J_{SC}$ [mA $cm^{-2}$] | $V_{OC}$ [V] | FF [%] | $PCE_{max}$[b] [%] | $R_{Sh}$[c] [Ω $cm^2$] | $R_S$[c] [Ω $cm^2$] |
|---|---|---|---|---|---|---|---|---|
| PM6[d]/BTP-4Cl-12 | 4.7 | HTL Solar[f] | 7.8 (7.5 ± 0.29) | 2.3 (2.2 ± 0.05) | 55.4 (55.1 ± 0.34) | 9.9 | 3848.7 | 87.4 |
| | 4.7 | HTL Solar[g] | 7.6 (7.5 ± 0.14) | 2.3 (2.2 ± 0.06) | 56.2 (55.9 ± 0.29) | 9.8 | 3994.2 | 89.3 |
| | 30.0 | HTL Solar[f] | 2.9 (2.6 ± 0.31) | 4.7 (4.6 ± 0.05) | 41.8 (41.5 ± 0.30) | 5.7 | 6927.9 | 561.3 |
| | 4.7 | h-HTL(W)[f] | 7.9 (7.7 ± 0.22) | 2.5 (2.5 ± 0.00) | 61.7 (61.5 ± 0.24) | 12.0 | 5501.7 | 82.1 |
| | 4.7 | h-HTL(W)[g] | 7.8 (7.7 ± 0.10) | 2.5 (2.5 ± 0.00) | 58.9 (58.7 ± 0.18) | 11.6 | 5427.3 | 86.7 |
| | 30.0 | h-HTL(W)[f] | 2.9 (2.7 ± 0.21) | 6.2 (6.1 ± 0.05) | 48.9 (48.7 ± 0.19) | 8.8 | 7337.3 | 528.3 |
| | 30.0 | h-HTL(W)[h] | 2.9 (2.6 ± 0.29) | 6.3 (6.3 ± 0.02) | 44.3 (44.0 ± 0.24) | 8.1 | 7137.8 | 532.3 |
| P(Cl−Cl)(BDD = 0.2)[e] /IT-4F | 4.7 | HTL Solar[f] | 8.2 (7.9 ± 0.25) | 2.6 (2.5 ± 0.07) | 43.4 (55.1 ± 0.34) | 9.2 | 2713.8 | 79.2 |
| | 4.7 | h-HTL(Mo)[f] | 8.3 (8.2 ± 0.13) | 2.7 (2.7 ± 0.03) | 49.2 (49.0 ± 0.17) | 11.0 | 3832.3 | 73.5 |

[a]Modules were fabricated with inverted structure (ITO/ZnO/photoactive layer/solution-processed HTLs/Ag, active area of 4.7 and 30.0 $cm^2$). [b]Maximum value was obtained from the best performance among fabricated modules. [c]$R_{Sh}$ and $R_S$ were calculated in the equivalent circuit. [d]PM6-based devices exhibited the best performance when composed of BTP-4Cl-12 (thermal treatment at 100 °C for 10 min). [e]P(Cl−Cl)(BDD = 0.2)-based devices exhibited the best performance when composed of IT-4F (thermal treatment at 140 °C for 10 min). [f]Modules were fabricated *via* the spin-coating process. [g]Modules were fabricated *via* the slot-die coating process. [h]Modules were fabricated *via* the all-solution process without any evaporation process.

contrast, the h-HTL(W) and h-HTL(Mo) films exhibited highly flattened surfaces, but slightly aggregated surfaces were observed due to the formation of metal oxides (Figure 5f,g). Therefore, the introduction of metal oxides improved the interfacial contact between the highly hydrophilic HTL Solar and hydrophobic photoactive layers, leading to good film formation with high conductivity.

The GIWAXS images and line-cut profiling graphs of the HTL films are shown in Figure 5h−k. Typically, HTL Solar has a perpendicular molecular orientation to the substrate, showing high conductivity.[66] The pristine HTL Solar film showed strong (100) peaks at $q_z$ of 0.33 $Å^{-1}$ along the out-of-plane direction, exhibiting a perpendicularly lamellar-stacked molecular structure (Figure 5h).[74,75] The peaks of PSS and PEDOT molecules were observed at 1.28 and 1.88 $Å^{-1}$, respectively, and the PEDOT peaks were lower in intensity than those of the PSS molecules, forming a crystalline structure unfavorable for good conductivity.[75] In contrast, h-HTL(W) and h-HTL(Mo) films exhibited strong (100) and (200) peaks at $q_z$ of 0.33 and 0.66 $Å^{-1}$, respectively, forming strong


https://doi.org/10.1021/acsami.1c01021
ACS Appl. Mater. Interfaces XXXX, XXX, XXX−XXX

lamellar-stacked structures compared to that of the pristine HTL Solar films. Furthermore, the peak intensity of the PEDOT molecules increased with the formation of h-HTLs, leading to a strong $\pi-\pi$ stacking of the PEDOT molecules. For deeper insights into the crystalline structure, the crystal coherence lengths of the peaks were calculated using the Scherrer equation for analyzing crystal size ($L_C$) (Table S9).[76] HTL Solar exhibited FWHM values of 0.495 and 0.307 Å$^{-1}$ along the $q_{xy}$ and $q_z$ axis with corresponding crystal sizes of 11.41 and 18.39 Å, respectively, which were domain sizes of PEDOT and PSS molecules. In contrast, h-HTL(W) and h-HTL(Mo) exhibited FWMH values of 0.426−0.427 and 0.280−0.283 Å$^{-1}$, which corresponded to crystal sizes of 13 and 20 Å, respectively. These results indicate that the h-HTLs formed strong aggregation of PEDOT molecules with a large domain. As a result, the formation of h-HTLs resulted in the formation of good morphology through the control of surface properties. Furthermore, h-HTL formation contributed to the enhancement of conductivity through the aggregation of PEDOT molecules.

**3.7. Solution Processable, Printable, and STP Large-Area Modules with h-HTLs.** For the successful commercialization of OSCs, the application of a solution process and large-area fabrication is necessary. In particular, for the development of high-performance large-area modules, good surface properties and high conductivity to overcome the thickness tolerance, as well as appropriate coating methods are the prerequisites.[25,77,78] The h-HTLs are suitable for large-area fabrication *via* a solution process owing to their good interfacial contact and high conductivities. In addition, based on the energy levels of the photoactive donors, energy-level matching can be facilitated by the introduction of suitable metal oxides. The images and photovoltaic properties of solution processable and printable large-area modules are shown in Figures 6 and S20 and Table 2. As shown in Figure 6a, the fabricated modules have three- and eight-cell connection (two types of modules with an active area of 4.7 cm$^2$ with a three-cell connection and 30.0 cm$^2$ with an eight-cell connection), comprising P1 (active area) and P2 (dead area). To minimize P2, each layer was formed through a solution process, and then, the patterning process was performed to fabricate the modules. Thus, the geometrical FF of the fabricated large-area module was approximately 81.6%, exhibiting relatively higher FF comparable with unit devices.[79] In the modules fabricated using PM6-based photoactive layers with deep HOMO energy levels and h-HTL(W) (module #1), a maximum PCE of 12.0% was achieved, affording higher efficiency, $V_{OC}$, and FF than those of the pristine HTL Solar-based module (9.9%) (Figure 6b). Similarly, in the modules fabricated using the P(Cl−Cl)(BDD = 0.2) donors with low-lying HOMO energy levels and h-HTL(Mo) (module #2), a maximum PCE of 10.6% was achieved, resulting in a better performance than that of the pristine HTL Solar-module (9.2%) (Figure S20).

With these techniques, the large-area printable modules (active area of 30.0 cm$^2$) were fabricated with h-HTL(W) and printed-Ag electrode formed through bar coating (Figure 6c). Also, the large-area solution-processed modules (active area of 30.0 cm$^2$) were fabricated with h-HTL(W) and evaporated-Ag (Figure S21). The solution-processed modules and printable modules exhibited 8.8 and 8.1% of PCEs, respectively (Figures S21 and 6d). Both solution-processed and printed modules exhibited high photovoltaic properties resulting from enhanced electronic and physical properties of h-HTL(W). These high PCEs were higher than pristine HTL Solar-incorporated modules (Table 2) and had comparable levels with the modules fabricated with e-$MoO_3$, resulting from high photovoltaic factors, especially $V_{OC}$ and FF (Table S10).

For extending applications of large-area modules, the STP modules (active area of 30.0 cm$^2$) were fabricated by introducing h-HTL(W) and the reported STP electrode.[5,80,81] The STP modules were fabricated with an inverted structure (ITO/ZnO/photoactive layer/h-HTL(W)/Au/Ag). The photovoltaic properties are shown in Figure 6d and Table S11, and the picture of fabricated STP modules is shown in Figure 6e. The STP modules exhibited 7.2% of PCE with high $V_{OC}$ and FF, similar tendency with solution-processed and printable modules. The average visible transmittance (AVT) values were calculated from the test method of KS L 2514. The formulae and measured factors are explained in Supporting Information.[82] The calculated AVT value of h-HTL(W)-incorporated STP electrodes was approximately 59.09% which was higher than those of the pristine STP electrodes with 49.38% (in Figure S22). This higher AVT value of h-HTL(W)-incorporated STP electrodes resulted from the high refractive index of the $WO_3$ layer, affording optically higher transparency.[83,84] As a result, the fabricated STP module exhibited approximately 22.30% of AVT at $\lambda$ = 380−780 nm (Figure S23).

With the introduction of suitable h-HTLs on the respective photoactive layers, energy-level matching was achieved with an increase in the interfacial contact, thereby resulting in enhanced conductivity. Consequently, the introduction of the h-HTLs resolved the issue of energy level mismatch in NFA-based OSCs and large-area modules, and enhanced electronic properties were obtained *via* a simple process. Furthermore, the h-HTLs have high potential for boosting transparency of STP electrodes with high transmittance properties. Considering these advantages, the h-HTLs can be potentially applied to the large-area, STP, and flexible modules, indicating their versatile applicability in various fields of organic electronics.

## 4. CONCLUSIONS

In this study, for the fabrication of high-performance NFA-based large-area OSCs and modules *via* a solution process, the h-HTLs incorporating $WO_3$ and $MoO_3$ were developed. The h-HTLs formed structures with a stoichiometrically small amount of oxygen vacancies (forming $W^{6+}$ and $Mo^{6+}$ structures) from the $W^{5+}$ and $Mo^{5+}$ structures formed n-doping states by solution-processed HTLs. This was attributed to the changes in the electronic structures owing to the high electronegativities of W and Mo atoms. The h-HTLs controlled the HOMO energy levels by variation of the contents of metal oxides, and then they could be applicable regardless of energy levels of the NFA-based photoactive layer. In addition, the h-HTL formation led to enhanced conductivity because of suitable interfacial matching and strong $\pi-\pi$ stacking of the PEDOT molecules. As a result, in the NFA-based photoactive layer, PCEs of up to 14.2% were obtained using h-HTLs in unit cells. Furthermore, PCEs of up to 12.0% were achieved in the modules (active area of 4.7 cm$^2$), demonstrating excellent device-to-module transfer. Also, the solution-processed modules and printable modules (active area of 30 cm$^2$) exhibited 8.8 and 8.1% of PCEs, resulting from enhanced electronic and physical properties of h-HTLs. Finally, for extended application of large-area modules, the


https://doi.org/10.1021/acsami.1c01021
ACS Appl. Mater. Interfaces XXXX, XXX, XXX−XXX

STP modules (active area of 30 $cm^2$) were successfully fabricated by introducing h-HTLs and STP electrodes, exhibiting 7.2% of PCE and 22.30% of AVT in $\lambda$ = 380−780 nm range. These results indicate that the devices and modules can be fabricated through a simple solution process, regardless of the types of the NFA-based photoactive layer. Furthermore, the developed method can be applied to the next-generation organic electronics and flexible modules based on the solution processes.

## ■ ASSOCIATED CONTENT

### Supporting Information

The Supporting Information is available free of charge at https://pubs.acs.org/doi/10.1021/acsami.1c01021.

Experimental data of $J-V$ curves of evaporated cells, energy level variations and alignments with content concentration of h-HTLs, carrier dissociation, conductivity, contact angles, photovoltaic properties of modules, transmittance, and AVT characteristics of STP modules and electrodes (PDF)

## ■ AUTHOR INFORMATION


### Corresponding Author

**Doo Kyung Moon** − *Nano and Information Materials Lab. (NIMs Lab.), Department of Chemical Engineering, Konkuk University, Seoul 05029, Republic of Korea;* orcid.org/0000-0001-9482-7508; Phone: +82-2-450-3498; Email: dkmoon@konkuk.ac.kr; Fax: +82-2-444-0765

### Authors

**Yong Woon Han** − *Nano and Information Materials Lab. (NIMs Lab.), Department of Chemical Engineering and The Academy of Applied Science and Technology, Konkuk University, Seoul 05029, Republic of Korea*

**Hyoung Seok Lee** − *Nano and Information Materials Lab. (NIMs Lab.), Department of Chemical Engineering, Konkuk University, Seoul 05029, Republic of Korea*

Complete contact information is available at: https://pubs.acs.org/10.1021/acsami.1c01021


### Author Contributions

[§]Y.W.H. and H.S.L. contributed equally to this work. The manuscript was written through contributions of all authors. All authors have given approval to the final version of the manuscript.

### Notes

The authors declare no competing financial interest.

## ■ ACKNOWLEDGMENTS

This research was supported by the New and Renewable Energy Core Technology Programs (grant nos. 2018201010636A and 20193091010110) and Human Resource Program (grant no. 20194010201790) of the Korea Institute of Energy Technology Evaluation and Planning (KETEP) grant funded by the Ministry of Trade, Industry and Energy (MOTIE) of Republic of Korea. This paper was written as part of Konkuk University's research support program for its faculty on sabbatical leave in 2018.

## ■ REFERENCES

(1) Sun, R.; Wu, Q.; Guo, J.; Wang, T.; Wu, Y.; Qiu, B.; Luo, Z.; Yang, W.; Hu, Z.; Guo, J.; Shi, M.; Yang, C.; Huang, F.; Li, Y.; Min, J. A Layer-by-Layer Architecture for Printable Organic Solar Cells Overcoming the Scaling Lag of Module Efficiency. *Joule* **2020**, *4*, 407−419.

(2) Meng, X.; Zhang, L.; Xie, Y.; Hu, X.; Xing, Z.; Huang, Z.; Liu, C.; Tan, L.; Zhou, W.; Sun, Y.; Ma, W.; Chen, Y. A General Approach for Lab-to-Manufacturing Translation on Flexible Organic Solar Cells. *Adv. Mater.* **2019**, *31*, 1903649.

(3) Sun, L.; Zeng, W.; Xie, C.; Hu, L.; Dong, X.; Qin, F.; Wang, W.; Liu, T.; Jiang, X.; Jiang, Y.; Zhou, Y. Flexible All-Solution-Processed Organic Solar Cells with High-Performance Nonfullerene Active Layers. *Adv. Mater.* **2020**, *32*, 1907840.

(4) Han, Y. W.; Jeon, S. J.; Lee, H. S.; Park, H.; Kim, K. S.; Lee, H. W.; Moon, D. K. Evaporation-Free Nonfullerene Flexible Organic Solar Cell Modules Manufactured by An All-Solution Process. *Adv. Energy Mater.* **2019**, *9*, 1902065.

(5) Zhong, J.; Xiao, Z.; Liang, W.; Wu, Y.; Ye, Q.; Xu, H.; Deng, H.; Shen, L.; Feng, X.; Long, Y. Highly Efficient and High Peak Transmittance Colorful Semitransparent Organic Solar Cells with Hybrid-Electrode-Mirror Microcavity Structure. *ACS Appl. Mater. Interfaces* **2019**, *11*, 47992−48001.

(6) Liu, Q.; Jiang, Y.; Jin, K.; Qin, J.; Xu, J.; Li, W.; Xiong, J.; Liu, J.; Xiao, Z.; Sun, K.; Yang, S.; Zhang, X.; Ding, L. 18% Efficiency Organic Solar Cells. *Sci. Bull.* **2020**, *65*, 272−275.

(7) Cui, Y.; Yao, H.; Zhang, J.; Xian, K.; Zhang, T.; Hong, L.; Wang, Y.; Xu, Y.; Ma, K.; An, C.; He, C.; Wei, Z.; Gao, F.; Hou, J. Single-Junction Organic Photovoltaic Cells with Approaching 18% Efficiency. *Adv. Mater.* **2020**, *32*, 1908205.

(8) Lin, Y.; Firdaus, Y.; Isikgor, F. H.; Nugraha, M. I.; Yengel, E.; Harrison, G. T.; Hallani, R.; El-Labban, A.; Faber, H.; Ma, C.; Zheng, X.; Subbiah, A.; Howells, C. T.; Bakr, O. M.; McCulloch, I.; De Wolf, S.; Tsetseris, L.; Anthopoulos, T. D. Self-Assembled Monolayer Enables Hole Transport Layer-Free Organic Solar Cells with 18% Efficiency and Improved Operational Stability. *ACS Energy Lett.* **2020**, *5*, 2935−2944.

(9) Lin, Y.; Adilbekova, B.; Firdaus, Y.; Yengel, E.; Faber, H.; Sajjad, M.; Zheng, X.; Yarali, E.; Seitkhan, A.; Bakr, O. M.; El-Labban, A.; Schwingenschlögl, U.; Tung, V.; McCulloch, I.; Laquai, F.; Anthopoulos, T. D. 17% Efficient Organic Solar Cells Based on Liquid Exfoliated $WS_2$ as a Replacement for PEDOT:PSS. *Adv. Mater.* **2019**, *31*, 1902965.

(10) Firdaus, Y.; Le Corre, V. M.; Khan, J. I.; Kan, Z.; Laquai, F.; Beaujuge, P. M.; Anthopoulos, T. D. Key Parameters Requirements for Non-Fullerene-Based Organic Solar Cells with Power Conversion Efficiency >20%. *Adv. Sci.* **2019**, *6*, 1802028.

(11) Gertsen, A. S.; Castro, M. F.; Søndergaard, R. R.; Andreasen, J. W. Scalable Fabrication of Organic Solar Cells Based on Non-Fullerene Acceptors. *Flexible Printed Electron.* **2020**, *5*, 014004.

(12) Wang, G.; Zhang, J.; Yang, C.; Wang, Y.; Xing, Y.; Adil, M. A.; Yang, Y.; Tian, L.; Su, M.; Shang, W.; Lu, K.; Shuai, Z.; Wei, Z. Synergistic Optimization Enables Large-Area Flexible Organic Solar Cells to Maintain over 98% PCE of the Small-Area Rigid Devices. *Adv. Mater.* **2020**, *32*, No. e2005153.

(13) Dong, S.; Jia, T.; Zhang, K.; Jing, J.; Huang, F. Single-Component Non-Halogen Solvent-Processed High-Performance Organic Solar Cell Module with Efficiency over 14%. *Joule* **2020**, *4*, 2004−2016.

(14) Gao, K.; Kan, Y.; Chen, X.; Liu, F.; Kan, B.; Nian, L.; Wan, X.; Chen, Y.; Peng, X.; Russell, T. P.; Cao, Y.; Jen, A. K. Y. Low-Bandgap Porphyrins for Highly Efficient Organic Solar Cells: Materials, Morphology, and Applications. *Adv. Mater.* **2020**, *32*, 1906129.

(15) Cai, F.; Peng, H.; Chen, H.; Yuan, J.; Hai, J.; Lau, T.-K.; Wang, J.; Hu, Y.; Liu, W.; Lu, X.; Zou, Y. An Asymmetric Small Molecule Acceptor for Organic Solar Cells with a Short Circuit Current Density over 24 mA $cm^{-2}$. *J. Mater. Chem. A* **2020**, *8*, 15984−15991.

(16) Zhang, J.; Wang, S.; Liu, Q.; Liu, Z.; Peng, R.; Ge, Z. HOMO Energy Level Regulation of Novel Conjugated Copolymers for Polymer Solar Cells. *New J. Chem.* **2015**, *39*, 6548−6554.

(17) Fan, B.; Zhang, D.; Li, M.; Zhong, W.; Zeng, Z.; Yang, L.; Huang, F.; Cao, Y. Achieving over 16% Efficiency for Single-Junction Organic Solar Cells. *Sci. China: Chem.* **2019**, *62*, 746−752.
(18) Wang, J.; Xu, H.; Xiao, Y.; Li, T.; Wang, J.; Liu, K.; Lu, X.; Zhan, X.; Chen, X. A Thiophene-Fused Benzotriazole Unit as a "$\pi$-Bridge" in A-$\pi$-D-$\pi$-A Type Acceptor to Achieve More Balanced $J_{SC}$ and $V_{OC}$ for OSCs. *Org. Electron.* **2020**, *82*, 105705.
(19) Sun, L.; Xu, X.; Song, S.; Zhang, Y.; Miao, C.; Liu, X.; Xing, G.; Zhang, S. Medium-Bandgap Conjugated Polymer Donors for Organic Photovoltaics. *Macromol. Rapid Commun.* **2019**, *40*, 1900074.
(20) Bin, H.; Zhong, L.; Yang, Y.; Gao, L.; Huang, H.; Sun, C.; Li, X.; Xue, L.; Zhang, Z.-G.; Zhang, Z.; Li, Y. Medium Bandgap Polymer Donor Based on Bi(Trialkylsilylthienyl-Benzo[1,2-b:4,5-B″]-Difuran) for High Performance Nonfullerene Polymer Solar Cells. *Adv. Energy Mater.* **2017**, *7*, 1700746.
(21) Liu, Q.; Jin, K.; Li, W.; Xiao, Z.; Cheng, M.; Yuan, Y.; Shi, S.; Jin, Z.; Hao, F.; Yang, S.; Ding, L. An Efficient Medium-Bandgap Nonfullerene Acceptor for Organic Solar Cells. *J. Mater. Chem. A* **2020**, *8*, 8857−8861.
(22) Wang, Y.; Wang, Y.; Zhu, L.; Liu, H.; Fang, J.; Guo, X.; Liu, F.; Tang, Z.; Zhang, M.; Li, Y. A Novel Wide-Bandgap Small Molecule Donor for High Efficiency All-Small-Molecule Organic Solar Cells with Small Non-Radiative Energy Losses. *Energy Environ. Sci.* **2020**, *13*, 1309−1317.
(23) Yao, J.; Qiu, B.; Zhang, ZG; Xue, L.; Wang, R.; Zhang, C.; Chen, S.; Zhou, Q.; Sun, C.; Yang, C.; Xiao, M.; Meng, L.; Li, Y. Cathode Engineering with Perylene-Diimide Interlayer Enabling over 17% Efficiency Single-Junction Organic Solar Cells. *Nat. Commun.* **2020**, *11*, 2726.
(24) Yang, B.; Chen, Y.; Cui, Y.; Liu, D.; Xu, B.; Hou, J. Over 100-Nm-Thick MoOx Films with Superior Hole Collection and Transport Properties for Organic Solar Cells. *Adv. Energy Mater.* **2018**, *8*, 1800698.
(25) Angmo, D.; Peng, X.; Cheng, J.; Gao, M.; Rolston, N.; Sears, K.; Zuo, C.; Subbiah, J.; Kim, S.-S.; Weerasinghe, H.; Dauskardt, R. H.; Vak, D. Beyond Fullerenes: Indacenodithiophene-Based Organic Charge-Transport Layer toward Upscaling of Low-Cost Perovskite Solar Cells. *ACS Appl. Mater. Interfaces* **2018**, *10*, 22143−22155.
(26) Xiong, S.; Hu, L.; Hu, L.; Sun, L.; Qin, F.; Liu, X.; Fahlman, M.; Zhou, Y. 12.5% Flexible Nonfullerene Solar Cells by Passivating the Chemical Interaction Between the Active Layer and Polymer Interfacial Layer. *Adv. Mater.* **2019**, *31*, No. e1806616.
(27) Han, Y. W.; Song, H. J.; Jeon, S. J.; Lee, H. S.; Ko, E. J.; Song, C. E.; Sung, T. H.; Moon, D. K. Excellent Carrier Transport Materials Produced by Controlled Molecular Stacking and Their Application in Flexible Organic Electronic Devices. *J. Mater. Chem. A* **2019**, *7*, 14790−14805.
(28) Kang, Q.; Yang, B.; Xu, Y.; Xu, B.; Hou, J. Printable MoOx Anode Interlayers for Organic Solar Cells. *Adv. Mater.* **2018**, *30*, 1801718.
(29) Cui, M.; Li, D.; Du, X.; Li, N.; Rong, Q.; Li, N.; Shui, L.; Zhou, G.; Wang, X.; Brabec, C. J.; Nian, L. A Cost-Effective, Aqueous-Solution-Processed Cathode Interlayer Based on Organosilica Nanodots for Highly Efficient and Stable Organic Solar Cells. *Adv. Mater.* **2020**, *32*, 2002973.
(30) Fan, X.; Nie, W.; Tsai, H.; Wang, N.; Huang, H.; Cheng, Y.; Wen, R.; Ma, L.; Yan, F.; Xia, Y. PEDOT:PSS for Flexible and Stretchable Electronics: Modifications, Strategies, and Applications. *Adv. Sci.* **2019**, *6*, 1900813.
(31) Li, Q.; Sun, Y.; Yang, C.; Liu, K.; Islam, M. R.; Li, L.; Wang, Z.; Qu, S. Optimizing the Component Ratio of PEDOT:PSS by Water Rinse for High Efficiency Organic Solar Cells over 16.7%. *Sci. Bull.* **2020**, *65*, 747−752.
(32) Son, H. J.; Park, H.-K.; Moon, J. Y.; Ju, B.-K.; Kim, S. H. Thermal Degradation Related to the PEDOT:PSS Hole Transport Layer and Back Electrode of the Flexible Inverted Organic Photovoltaic Module. *Sustainable Energy Fuels* **2020**, *4*, 1974−1983.
(33) Lim, F. J.; Ananthanarayanan, K.; Luther, J.; Ho, G. W. Influence of a Novel Fluorosurfactant Modified PEDOT:PSS Hole Transport Layer on the Performance of Inverted Organic Solar Cells. *J. Mater. Chem.* **2012**, *22*, 25057−25064.
(34) Teng, N. W.; Li, C. H.; Lo, W. C.; Tsai, Y. S.; Liao, C. Y.; You, Y. W.; Ho, H. L.; Li, W. L.; Lee, C. C.; Lin, W. C.; Chang, Y. M. Highly Efficient Nonfullerene Organic Photovoltaic Devices with 10% Power Conversion Efficiency Enabled by a Fine-Tuned and Solution-Processed Hole-Transporting Layer. *Sol. RRL* **2020**, *4*, 2000223.
(35) Norrman, K.; Madsen, M. V.; Gevorgyan, S. A.; Krebs, F. C. Degradation Patterns in Water and Oxygen of an Inverted Polymer Solar Cell. *J. Am. Chem. Soc.* **2010**, *132*, 16883−16892.
(36) Zeng, W.; Xie, C.; Wang, W.; Li, S.; Jiang, X.; Xiong, S.; Sun, L.; Qin, F.; Han, H.; Zhou, Y. Incorporation of Hydrogen Molybdenum Bronze in Solution-Processed Interconnecting Layer for Efficient Nonfullerene Tandem Organic Solar Cells. *Sol. RRL* **2020**, *4*, 1900480.
(37) Maisch, P.; Eisenhofer, L. M.; Tam, K. C.; Distler, A.; Voigt, M. M.; Brabec, C. J.; Egelhaaf, H.-J. A Generic Surfactant-Free Approach to Overcome Wetting Limitations and Its Application to Improve Inkjet-Printed P3HT:Non-Fullerene Acceptor PV. *J. Mater. Chem. A* **2019**, *7*, 13215−13224.
(38) Qiu, W.; Müller, R.; Voroshazi, E.; Conings, B.; Carleer, R.; Boyen, H.-G.; Turbiez, M.; Froyen, L.; Heremans, P.; Hadipour, A. Nafion-Modified MoOx as Effective Room-Temperature Hole Injection Layer for Stable, High-Performance Inverted Organic Solar Cells. *ACS Appl. Mater. Interfaces* **2015**, *7*, 3581−3589.
(39) Chen, L.; Xie, C.; Chen, Y. Optimization of the Power Conversion Efficiency of Room Temperature-Fabricated Polymer Solar Cells Utilizing Solution Processed Tungsten Oxide and Conjugated Polyelectrolyte as Electrode Interlayer. *Adv. Funct. Mater.* **2014**, *24*, 3986−3995.
(40) Gong, Y.; Dong, Y.; Zhao, B.; Yu, R.; Hu, S.; Tan, Z. a. Diverse Applications of MoO3 for High Performance Organic Photovoltaics: Fundamentals, Processes and Optimization Strategies. *J. Mater. Chem. A* **2020**, *8*, 978−1009.
(41) Zheng, H.; Ou, J. Z.; Strano, M. S.; Kaner, R. B.; Mitchell, A.; Kalantar-zadeh, K. Nanostructured Tungsten Oxide - Properties, Synthesis, and Applications. *Adv. Funct. Mater.* **2011**, *21*, 2175−2196.
(42) Wang, Y.; Luo, Q.; Wu, N.; Wang, Q.; Zhu, H.; Chen, L.; Li, Y.-Q.; Luo, L.; Ma, C.-Q. Solution-Processed MoO3:PEDOT:PSS Hybrid Hole Transporting Layer for Inverted Polymer Solar Cells. *ACS Appl. Mater. Interfaces* **2015**, *7*, 7170−7179.
(43) Jeon, S. J.; Han, Y. W.; Moon, D. K. 13.9%-Efficiency and Eco-Friendly Nonfullerene Polymer Solar Cells Obtained by Balancing Molecular Weight and Solubility in Chlorinated Thiophene-Based Polymer Backbones. *Small* **2019**, *15*, No. e1902598.
(44) Ho, C. H. Y.; Kim, T.; Xiong, Y.; Firdaus, Y.; Yi, X.; Dong, Q.; Rech, J. J.; Gadisa, A.; Booth, R.; O'Connor, B. T.; Amassian, A.; Ade, H.; You, W.; Anthopoulos, T. D.; So, F. High-Performance Tandem Organic Solar Cells Using HSolar as the Interconnecting Layer. *Adv. Energy Mater.* **2020**, *10*, 2000823.
(45) Ouyang, J. "secondary Doping" Methods to Significantly Enhance the Conductivity of PEDOT:PSS for Its Application as Transparent Electrode of Optoelectronic Devices. *Displays* **2013**, *34*, 423−436.
(46) Hosseini, E.; Ozhukil Kollath, V.; Karan, K. The Key Mechanism of Conductivity in PEDOT:PSS Thin Films Exposed by Anomalous Conduction Behaviour upon Solvent-Doping and Sulfuric Acid Post-Treatment. *J. Mater. Chem. C* **2020**, *8*, 3982−3990.
(47) Wang, J.; Yu, H.; Hou, C.; Zhang, J. Solution-Processable PEDOT:PSS:$\alpha$-In2Se3 with Enhanced Conductivity as a Hole Transport Layer for High-Performance Polymer Solar Cells. *ACS Appl. Mater. Interfaces* **2020**, *12*, 26543−26554.
(48) Migliaccio, L.; Altamura, D.; Scattarella, F.; Giannini, C.; Manini, P.; Gesuele, F.; Maglione, M. G.; Tassini, P.; Pezzella, A. Impact of Eumelanin−PEDOT Blending: Increased PEDOT Crystalline Order and Packing−Conductivity Relationship in Ternary PEDOT:PSS:Eumelanin Thin Films. *Adv. Electron. Mater.* **2019**, *5*, 1800585.


https://doi.org/10.1021/acsami.1c01021
ACS Appl. Mater. Interfaces XXXX, XXX, XXX−XXX

(49) Xu, B.; Gopalan, S. A.; Gopalan, A. I.; Muthuchamy, N.; Lee, K. P.; Lee, J. S.; Jiang, Y.; Lee, S. W.; Kim, S. W.; Kim, J. S.; Jeong, H. M.; Kwon, J. B.; Bae, J. H.; Kang, S. W. Functional Solid Additive Modified PEDOT:PSS as an Anode Buffer Layer for Enhanced Photovoltaic Performance and Stability in Polymer Solar Cells. *Sci. Rep.* **2017**, *7*, 45079.
(50) Lee, Y.-J.; Lee, T.; Soon, A. Phase Stability Diagrams of Group 6 Magnéli Oxides and Their Implications for Photon-Assisted Applications. *Chem. Mater.* **2019**, *31*, 4282−4290.
(51) Ingham, B.; Hendy, S. C.; Chong, S. V.; Tallon, J. L. Density-Functional Studies of Tungsten Trioxide, Tungsten Bronzes, and Related Systems. *Phys. Rev. B: Condens. Matter Mater. Phys.* **2005**, *72*, 075109.
(52) Khalate, S. A.; Kate, R. S.; Pathan, H. M.; Deokate, R. J. Structural and Electrochemical Properties of Spray Deposited Molybdenum Trioxide ($\alpha$-MoO3) Thin Films. *J. Solid State Electrochem.* **2017**, *21*, 2737−2746.
(53) Galatsis, K.; Li, Y. X.; Wlodarski, W.; Kalantar-zadeh, K. Sol-Gel Prepared MoO3-WO3 Thin-Films for O2 Gas Sensing. *Sens. Actuators, B* **2001**, *77*, 478−483.
(54) Lee, M.-H.; Chen, L.; Li, N.; Zhu, F. MoO3-Induced Oxidation Doping of PEDOT:PSS for High Performance Full-Solution-Processed Inverted Quantum-Dot Light Emitting Diodes. *J. Mater. Chem. C* **2017**, *5*, 10555−10561.
(55) Luo, Y. Bond Dissociation Energies. In *CRC Handbook of Chemistry and Physics*; 2009; Vol. *9*.
(56) Wang, Y.; Lan, W.; Li, N.; Lan, Z.; Li, Z.; Jia, J.; Zhu, F. Stability of Nonfullerene Organic Solar Cells: From Built-in Potential and Interfacial Passivation Perspectives. *Adv. Energy Mater.* **2019**, *9*, 1900157.
(57) Cheng, J.; Xie, F.; Liu, Y.; Sha, W. E. I.; Li, X.; Yang, Y.; Choy, W. C. H. Efficient Hole Transport Layers with Widely Tunable Work Function for Deep HOMO Level Organic Solar Cells. *J. Mater. Chem. A* **2015**, *3*, 23955−23963.
(58) Wang, F.; Wang, Y.; Liu, H.; Hu, S.; Liu, J.; Liu, L.; Bai, Y.; Hayat, T.; Alsaedi, A.; Tan, Z. a. Fine Tuning the Light Distribution within the Photoactive Layer by Both Solution-Processed Anode and Cathode Interlayers for High Performance Polymer Solar Cells. *Sol. RRL* **2018**, *2*, 1800141.
(59) Graetzel, M.; Janssen, R. A. J.; Mitzi, D. B.; Sargent, E. H. Materials Interfaces Engineering for Solution-Processed Photovoltaics. *Nature* **2012**, *488*, 304−312.
(60) Han, Y. W.; Jung, C. H.; Lee, H. S.; Jeon, S. J.; Moon, D. K. High-Performance Nonfullerene Organic Photovoltaics Applicable for Both Outdoor and Indoor Environments through Directional Photon Energy Transfer. *ACS Appl. Mater. Interfaces* **2020**, *12*, 38470−38482.
(61) Duan, L.; Zhang, Y.; Yi, H.; Haque, F.; Deng, R.; Guan, H.; Zou, Y.; Uddin, A. Trade-Off between Exciton Dissociation and Carrier Recombination and Dielectric Properties in Y6-Sensitized Nonfullerene Ternary Organic Solar Cells. *Energy Technol.* **2020**, *8*, 1900924.
(62) Tang, Y.; Bjuggren, J. M.; Fei, Z.; Andersson, M. R.; Heeney, M.; McNeill, C. R. Origin of Open-Circuit Voltage Turnover in Organic Solar Cells at Low Temperature. *Sol. RRL* **2020**, *4*, 2000375.
(63) Qi, B.; Wang, J. Open-Circuit Voltage in Organic Solar Cells. *J. Mater. Chem.* **2012**, *22*, 24315−24325.
(64) Amorim, D. R. B.; Coutinho, D. J.; Miranda, P. B.; Faria, R. M. Analytical Model for Photocurrent in Organic Solar Cells as a Function of the Charge-Transport Figure of Merit Including Second-Order Recombination. *Phys. Rev. Appl.* **2020**, *14*, 034046.
(65) Destouesse, E.; Chambon, S.; Courtel, S.; Hirsch, L.; Wantz, G. Solution-Processed Small-Molecule Bulk Heterojunctions: Leakage Currents and the Dewetting Issue for Inverted Solar Cells. *ACS Appl. Mater. Interfaces* **2015**, *7*, 24663−24669.
(66) Na, S.-I.; Wang, G.; Kim, S.-S.; Kim, T.-W.; Oh, S.-H.; Yu, B.-K.; Lee, T.; Kim, D.-Y. Evolution of Nanomorphology and Anisotropic Conductivity in Solvent-Modified PEDOT:PSS Films for Polymeric Anodes of Polymer Solar Cells. *J. Mater. Chem.* **2009**, *19*, 9045−9053.
(67) Liu, Y.; Zhao, Y.; Xu, S.; Cao, S. Enhanced Electroluminescent Efficiency with Ionic Liquid Doped into PEDOT:PSS Hole-Injecting Layer. *Polymer* **2015**, *77*, 42−47.
(68) Hiate, T.; Miyauchi, N.; Liu, Q.; Ishikawa, R.; Ueno, K.; Shirai, H. Real-Time Measurement of Optical Anisotropy during Film Growth Using a Chemical Mist Deposition of Poly(3,4-Ethylenedioxythiophene): Poly(Styrenesulfonate). *J. Appl. Phys.* **2014**, *115*, 123514.
(69) Qiu, H.; Lu, Y. F.; Mai, Z. H. Electrochromic Writing and Erasing on Tungsten Oxide Films in Air by Scanning Tunneling Microscopy. *J. Appl. Phys.* **2002**, *91*, 440−443.
(70) Wang, F.; Tan, Z. a.; Li, Y. Solution-Processable Metal Oxides/Chelates as Electrode Buffer Layers for Efficient and Stable Polymer Solar Cells. *Energy Environ. Sci.* **2015**, *8*, 1059−1091.
(71) Xie, F.; Choy, W. C. H.; Wang, C.; Li, X.; Zhang, S.; Hou, J. Low-Temperature Solution-Processed Hydrogen Molybdenum and Vanadium Bronzes for an Efficient Hole-Transport Layer in Organic Electronics. *Adv. Mater.* **2013**, *25*, 2051−2055.
(72) Han, Y. W.; Choi, J. Y.; Lee, Y. J.; Ko, E. J.; Choi, M. H.; Suh, I. S.; Moon, D. K. Vertical Phase Separation for Highly Efficient Organic Solar Cells Incorporating Conjugated-Polyelectrolytes. *Adv. Mater. Interfaces* **2019**, *6*, 1801396.
(73) Honda, S.; Ohkita, H.; Benten, H.; Ito, S. Selective Dye Loading at the Heterojunction in Polymer/Fullerene Solar Cells. *Adv. Energy Mater.* **2011**, *1*, 588−598.
(74) Petsagkourakis, I.; Pavlopoulou, E.; Portale, G.; Kuropatwa, B. A.; Dilhaire, S.; Fleury, G.; Hadziioannou, G. Structurally-Driven Enhancement of Thermoelectric Properties within Poly(3,4-Ethylenedioxythiophene) Thin Films. *Sci. Rep.* **2016**, *6*, 30501.
(75) Wang, Y.; Zhu, C.; Pfattner, R.; Yan, H.; Jin, L.; Chen, S.; Molina-Lopez, F.; Lissel, F.; Liu, J.; Rabiah, N. I.; Chen, Z.; Chung, J. W.; Linder, C.; Toney, M. F.; Murmann, B.; Bao, Z. A Highly Stretchable, Transparent, and Conductive Polymer. *Sci. Adv.* **2017**, *3*, No. e1602076.
(76) Xie, Y.; Li, T.; Guo, J.; Bi, P.; Xue, X.; Ryu, H. S.; Cai, Y.; Min, J.; Huo, L.; Hao, X.; Woo, H. Y.; Zhan, X.; Sun, Y. Ternary Organic Solar Cells with Small Nonradiative Recombination Loss. *ACS Energy Lett.* **2019**, *4*, 1196−1203.
(77) Bai, Y.; Zhao, C.; Zhang, S.; Zhang, S.; Yu, R.; Hou, J.; Tan, Z. a.; Li, Y. Printable SnO2 Cathode Interlayer with up to 500 Nm Thickness-Tolerance for High-Performance and Large-Area Organic Solar Cells. *Sci. China Chem.* **2020**, *63*, 957−965.
(78) Kang, Q.; Liao, Q.; Xu, Y.; Xu, L.; Zu, Y.; Li, S.; Xu, B.; Hou, J. P-Doping Conducting Polyelectrolytes as an Anode Interlayer Enables High Efficiency for 1 Cm2 Printed Organic Solar Cells. *ACS Appl. Mater. Interfaces* **2019**, *11*, 20205−20213.
(79) Strohm, S.; Machui, F.; Langner, S.; Kubis, P.; Gasparini, N.; Salvador, M.; McCulloch, I.; Egelhaaf, H. J.; Brabec, C. J. P3HT:Non-Fullerene Acceptor Based Large Area, Semi-Transparent PV Modules with Power Conversion Efficiencies of 5%, Processed by Industrially Scalable Methods. *Energy Environ. Sci.* **2018**, *11*, 2225−2234.
(80) Xu, G.; Shen, L.; Cui, C.; Wen, S.; Xue, R.; Chen, W.; Chen, H.; Zhang, J.; Li, H.; Li, Y.; Li, Y. High-Performance Colorful Semitransparent Polymer Solar Cells with Ultrathin Hybrid-Metal Electrodes and Fine-Tuned Dielectric Mirrors. *Adv. Funct. Mater.* **2017**, *27*, 1605908.
(81) Wang, S.; Chen, J.; Li, L.; Zuo, L.; Qu, T.-Y.; Ren, H.; Li, Y.; Jen, A. K.-Y.; Tang, J.-X. Narrow Bandpass and Efficient Semi-transparent Organic Solar Cells Based on Bioinspired Spectrally Selective Electrodes. *ACS Nano* **2020**, *14*, 5998−6006.
(82) Yang, C.; Liu, D.; Bates, M.; Barr, M. C.; Lunt, R. R. How to Accurately Report Transparent Solar Cells. *Joule* **2019**, *3*, 1803−1809.
(83) Zhang, X.; Wu, X.; Amrehn, S.; Wagner, T. Refractive Index Modulation in Metal Oxides Arising from Chemically Induced Free Carriers and Its Application in Gas Sensing. *J. Mater. Chem. C* **2019**, *7*, 6752−6758.


https://doi.org/10.1021/acsami.1c01021
ACS Appl. Mater. Interfaces XXXX, XXX, XXX−XXX

(84) Wang, Y.; He, B.; Wang, H.; Xu, J.; Li, W.; Wang, Q.; Yang, S. Transparent $WO_3$/Ag/$WO_3$ Electrode for Flexible Organic Solar Cells. *Mater. Lett.* **2017**, *188*, 107−110.



https://doi.org/10.1021/acsami.1c01021
*ACS Appl. Mater. Interfaces* XXXX, XXX, XXX−XXX